Journal of Materials Chemistry A

ROYAL SOCIETY OF CHEMISTRY

REVIEW

View Article Online
View Journal | View Issue

Cite this: J. Mater. Chem. A, 2024, 12, 12293

A review on passivation engineering for improving photocatalytic hydrogen evolution performance

Dandan Ma, Jiantao Chen, Jun Li, Xin Ji and Jian-Wen Shi *

Photocatalytic hydrogen evolution (PHE) is a promising route for the energy-renewable and eco-friendly development of the future society, but the low activity and durability of photocatalysts seriously restrict the development of this technology. In this case, passivation engineering may provide a feasible idea to solve these problems, by which a relatively stable and mild environment can be formed to guarantee the high separation and utilization of photogenerated charge carriers. Recently, passivation engineering has been increasingly adopted for improving the activity and durability of photocatalysts, and thus, a comprehensive review will help researchers understand and use this technology to construct high-performance photocatalytic systems. Herein, firstly, the basic concept and the roles of the passivation technique in PHE are discussed. Subsequently, we introduce the commonly utilized synthesis methods, followed by the characterization techniques employed in passivation engineering. Thereafter, we review the categories and mechanism of passivation engineering in PHE. Lastly, the challenges and perspectives of passivation engineering for future practical applications are discussed. We hope that this review can provide some useful guidance and trigger interest in passivation engineering for the construction of high-performance photocatalysts.

Received 18th January 2024
Accepted 12th April 2024

DOI: 10.1039/d4ta00411f

rsc.li/materials-a

1. Introduction

The development of sustainable energy is the focus of attention worldwide. In this case, photocatalytic hydrogen evolution (PHE) technology is capable of converting endless solar energy into clean hydrogen and thus is promising for driving the development and revolution of sustainable energy.[1–4] The key to the practical development and application of PHE technology is to find ideal photocatalysts that can efficiently and stably convert solar energy into hydrogen.[5,6] Many photocatalysts, such as single-component semiconductors (ZnO, TiO_2, CdS, ZnS, MoS_2, g-C_3N_4, *etc.*[7–15]) and hybrid systems consisting of two or three semiconductors (TiO_2@ZnO, CdS@g-C_3N_4, CdS/MoS_2, *etc.*[16–22]) have been reported to date. However, their limited photocatalytic activity and unsatisfactory stability are still the most significant issues.[16–19] The core task of developing high-performance photocatalysts is to suppress the harmful recombination of charge carriers, accelerate the surface reaction and prevent photocorrosion.

Accordingly, massive efforts, including morphological and structural design, ion doping, homojunction and heterojunction construction, and single atomic modification strategies,[23–27] have been devoted to improving the light absorption, charge transfer and surface reaction of photocatalysts in the past decades. However, an unshakable fact is that the use of each of the mentioned strategies often introduces new problems while solving one problem, thus failing to significantly improve the properties of the catalyst as expected. For example, single-component semiconductor photocatalysts suffer from serious charge recombination, which can be solved through the construction of a heterostructure, but the inadequate interface contact between different semiconductors results in harmful charge carrier recombination at the interface. Another example is that increasing the specific surface area of catalysts can undoubtedly provide more active sites for the hydrogen evolution reaction, but the exposure of these susceptible surfaces also results in more serious photocorrosion and more side reactions. Fortunately, this compensatory improvement in the performance of photocatalysts has been noticed by researchers, and they are actively looking for ways to establish a better balance to minimize potential negative impacts.

Among the numerous strategies, passivation technique may provide one of the most ideal solutions to the mentioned problems.[28,29] The passivation technique can be used to reduce the effect of photogenerated holes on the catalyst surface or provide additional protection for sensitive catalyst surfaces.[30–32] In other reports, passivation techniques can also release the stress between different semiconductors to guarantee the formation of high-quality interfaces.[33,34] However, to the best of our knowledge, there are scarce reviews thoroughly summarizing the application of the passivation technique in PHE

State Key Laboratory of Electrical Insulation and Power Equipment, Center of Nanomaterials for Renewable Energy, School of Electrical Engineering, Xi'an Jiaotong University, Xi'an 710049, China. E-mail: jianwen.shi@mail.xjtu.edu.cn

although this topic has been gaining continuous attention. This was a positive incentive for us to provide a comprehensive review to introduce the basic principle and recent progress in the passivation technique, which may provide ideas and design inspiration for researchers to further improve the activity and stability of photocatalysts.

This review aims to provide a panorama of passivation engineering over semiconductor-based composite photocatalysts and systematically summarize the progress in different passivation strategies in recent years. Initially, we present a brief introduction to the basic concept and the roles of passivation technique in PHE. Subsequently, we introduce the commonly utilized synthesis methods and characterization methods in passivation engineering. Then, we review the categories and mechanism of passivation engineering in PHE. Finally, the challenges and perspectives of passivation engineering for future practical applications are discussed.

2. The basic principles and roles of passivation engineering in PHE

Passivation is a material treatment method developed in the metal materials field, which initially refers to the phenomenon that after forming a thin layer of metal oxide on the surface of the active metal, the protection effect of the metal oxide makes it difficult for the inner metal to be further oxidized, thus displaying inert chemical properties.[35,36] Therefore, the direct role of the passivation technique is to shield the active and easily affected factors in the original system or remove them to improve the stability of the system.

As is known, catalytic reactions occur in dynamic and easily disturbed systems. As shown in Fig. 1, the continuous generation of electrons and holes, the unstable solid–liquid and solid–solid interfaces, the large exposure of active surface, and the presence of defects and vacancies create an environment in which the photocatalyst itself is easily destroyed by photocorrosion and the photogenerated charge carriers are easily quenched.[37,38] (1) The surface photogenerated holes and electrons may undergo harmful recombination before the REDOX reaction. (2) The PHE will decrease if the photogenerated electrons are trapped and quenched by defects. (3) The lifetime of photocatalysts will decrease due to photo-corrosion. (4) The competing side reactions consume electrons, resulting in a limited PHE performance. (5) The PHE activity can also be affected by the impurities adsorbed on the surface of photocatalysts. Thus, passivation engineering in PHE can be employed to prolong the service life of photocatalysts and improve their hydrogen evolution capacity by eliminating the above-mentioned potential negative factors.

2.1 Prolonging the service life of photocatalysts

Photo-corrosion is a long-term problem, where some light-sensitive photocatalysts will dissolve or undergo structural changes under light irradiation conditions, and thus lose their catalytic activity rapidly.[39–41] In this case, a passivation layer can provide extra protection to the light-sensitive component, suppress the corrosion reaction at the solid–liquid interface and reduce the instability of the solid–solid interface. In addition, the introduction of a passivation layer can create an inert environment to prevent the occurrence of adverse surface reactions and provide a relatively stable platform for the evolution of hydrogen, thus prolonging the lifetime of the photocatalyst (Fig. 2).[42,43]

2.2 Improving hydrogen evolution activity

Besides the accessible surface of the photocatalyst, its complex inner environment can also be improved by passivation techniques. During the past few decades, many researchers have focused on decreasing the harmful defects, vacancies, and interface disorders to suppress the recombination of charge carriers.[44,45] The passivation technique has been proven to be efficient in inhibiting the formation of harmful defects and releasing interface stress, thus creating a smooth channel for the transfer of photogenerated charge carriers from the inner to the surface reaction sites of the catalyst.[46,47]

3. Realization of passivation engineering

When passivation engineering is used to improve the activity and lifetime of a photocatalyst, it is necessary to carefully design

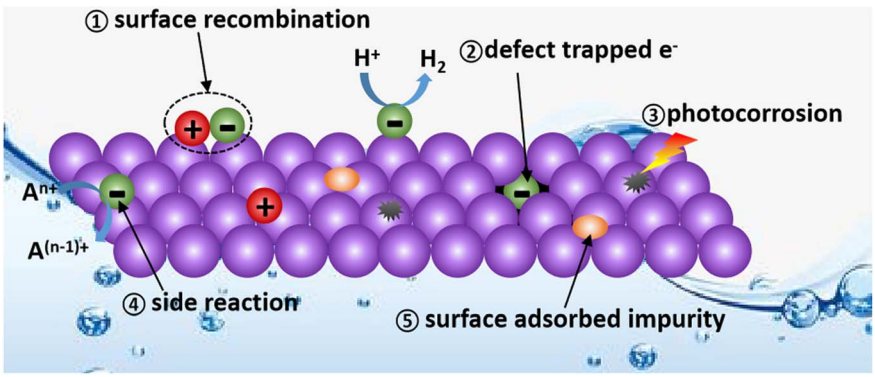

Fig. 1 Diagram of the possible factors decreasing the PHE activity of photocatalysts.

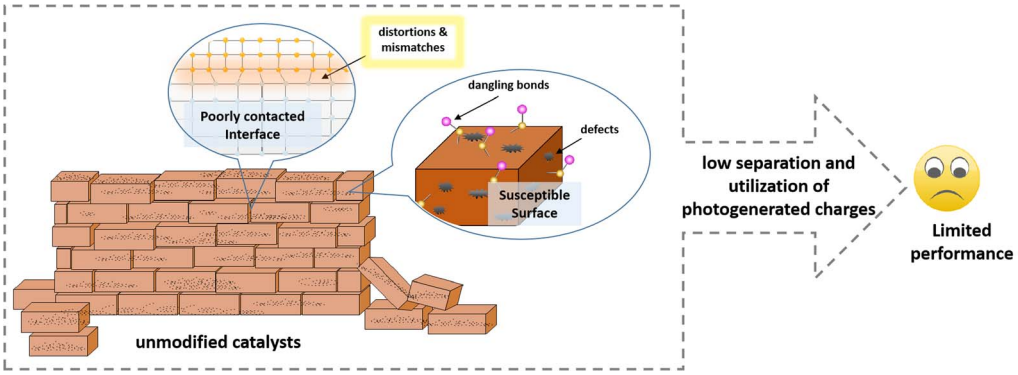

Fig. 2 Diagram of passivation engineering in improving the photocatalytic activity and durability.

and tailor it to create a stable and unobstructed reaction environment and minimize the potential negative impact of passivation engineering on the catalyst. Among the factors, the choice of an appropriate synthesis method plays the dominant role in guaranteeing the passivation effect. Here, the most commonly utilized synthesis methods will be introduced and discussed.

3.1 *In situ* reaction method

The *in situ* fabrication method is a widely used strategy in inserting a passivation layer between two different materials. For example, Dey and coworkers[48] fabricated a Cu_2O/CuO heterojunction using an atmospheric pressure plasma jet method (Fig. 3a), and in this process, CuO with a low density of interfacial defects can be formed from the surface of the Cu_2O base, and thus an intimately contacted heterostructure can be constructed. The catalytic performance and stability of the Cu_2O photocatalyst were significantly enhanced with the treatment plasma. Daskalakis and coworkers[49] treated a Cu-doped ZnS photocatalyst using a wet-chemical sulfidation process and obtained Cu_2S in the system (Fig. 3b). It was found that on a particular composite catalyst, the surface defect sites of Cu-ZnS can be passivated during the sulfidation process, in which sulfur vacancies were created from the charge compensation by Cu^+ substitution with Zn^{2+} sites, leading to improved charge transfer at the Cu_2S/ZnS interface, and thus the photocatalytic activity of Cu-ZnS could be largely improved. In addition, Alam *et al.*[50] passivated g-C_3N_4-S by loading BiOI nanoplates with carbon nitride structures through an *in situ* hydrothermal method (Fig. 3c). They found that the synergistic effect of trap passivation and charge separation in g-C_3N_4-S/BiOI efficiently resulted in a higher photocurrent and lower charge transfer resistance.

A similar design was also reported by Kang and coworkers,[51] where they introduced a thin film of black TiO_2 (BT) between TiO_2 and Au cocatalyst by using an *in situ* electrochemical anodization approach (Fig. 4a). The existence of BT guaranteed the highly-uniformed deposition of the Au cocatalyst on the top of the mesoporous TiO_2-BT nanotube array, resulting in a 10 times enhancement of the photocatalytic H_2 evolution reactivity over conventional TiO_2 nanotube (Fig. 4c and d). Compared with pure TiO_2, the heterojunction formed by TiO_2 and BT exhibited better photocatalytic ability because the TiO_2-BT interface had a good conduction band arrangement, which makes the transfer of electrons from the conduction band of TiO_2 to the conduction band of black TiO_2 easier and promotes the separation of electron–holes pairs. Thus, the black TiO_2 acts as a buffer layer for the TiO_2 conduction band electrons in the TiO_2-BT/Au system, which allows efficient photogenerated electrons to be transferred to Au nanoparticles, and then into the TiO_2 pores that suitable for H_2 generation (Fig. 4b).

During the *in situ* growth method, passivation materials nucleate and grow spontaneously from the body phase of the substrate materials, thus having good interface compatibility with the substrate materials, which greatly reduces the defects and stresses caused by the direct contact of different semiconductors. However, this method also faces shortcomings, as follows: (1) in the *in situ* growth method, some critical properties, such as crystallinity, species and thickness of the passivation layer, are difficult to control, although some reports attempted to regulate the properties of the passivation layer through the *in situ* synthesis conditions. (2) Limited by the properties of the substrate materials and the crystal growth process, the type of passivation layer can hardly be regulated by the *in situ* growth method.

3.2 Deposition method

To precisely control the type and thickness of the passivation layer, deposition methods, including atomic layer deposition (ALD), electrochemical deposition, electron beam evaporation, have been adopted in the past few decades, in which researchers not only can choose different types of passivation materials according to the need, but also control their thickness and crystallinity through the deposition conditions.[52–58] For example, Zhang *et al.*[52] covered an Al/Al_2O_3 passivation layer on the surface of TiO_2/Cu_2O hybrid substrate by using magnetron sputtering method (Fig. 5a), where the thickness of the deposited Al layers could be regulated to 10, 20, and 30 nm. Furthermore, ALD is a widely accepted method for the deposition of an ultrathin passivation layer, in which the thickness of the deposition layer can be controlled at the atomic level due to its self-limited growth character.[54–58] For example, the

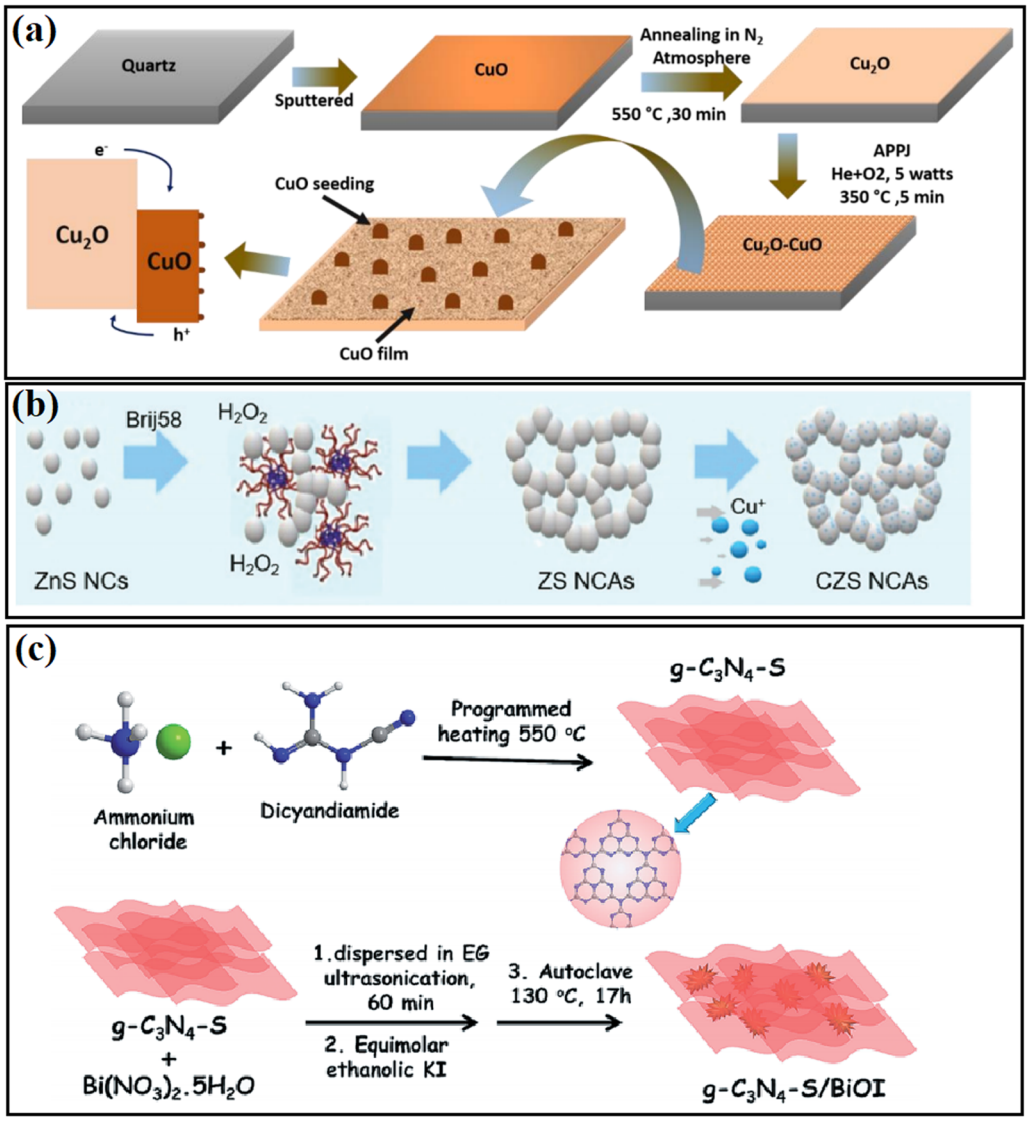

Fig. 3 (a) Flowchart of the synthesis process for the Cu_2O/CuO heterojunction electrode. Reproduced with permission from ref. 48. Copyright 2020, Elsevier. (b) Schematic representation of the synthesis of mesoporous ZnS (ZS) and Cu-doped ZnS (CZS) NC-linked assemblies (NCAs). Reproduced with permission from ref. 49. Copyright 2020, the Royal Society of Chemistry. (c) Synthetic strategy of g-C_3N_4-S/BiOI heterojunction composite using the *in situ* strategy. Reproduced with permission from ref. 50. Copyright 2019, the Royal Society of Chemistry.

conformal growth of a 1 nm-thick TiO_2 shell on ZnO NAs was realized using the ALD technique. Bai and coworkers[55] deposited a TiO_2 protection layer on the surface of a 3D Si nanowire trunk/ZnO nanowire branch (Fig. 5b) and found that a thin layer of TiO_2 could efficiently protect the photocatalyst from corrosion. To accelerate the separation of electrons and holes by improving the interface properties, Feng *et al.*[56] deposited a thin Al_2O_3 passivation layer between C QDs and TiO_2 NRs using the ALD technique (Fig. 5c). The highest H_2 evolution activity was obtained when the thickness of Al_2O_3 was 5 nm.

Also, our group[57] controlled the deposition thickness of the Al_2O_3 interlayer by tuning the deposition cycle from 1 to 10 and found that 2 cycles of Al_2O_3 deposition resulted in 1.1 times higher H_2 evolution ability than the sample without Al_2O_3 deposition. It was found that a too thin or too thick passivation layer was not conductive to the improvement in PHE activity. Usually, the transfer of charge carriers could be sped up through the tunneling effect when an interfacial passivation layer with a thickness of less than 2 nm was inserted,[54] but the ultrathin layer may increase the possibility of generating weak points, thus losing the partial passivation effect.

Chen *et al.*[58] discussed the influence of the fabrication method on the passivation effect of a TiO_2 seed layer by fabricating the layer using the spin coating (SC), magnetron sputtering (MS) and ALD methods. It was found that the different fabrication methods resulted in different crystallinity in the TiO_2 layer, which affected the band alignment between the semiconductors, and finally resulted in different PHE performances. Luo *et al.*[59] introduced a TiO_2 layer between FTO and Fe_2O_3 through the ALD method, where the deposited TiO_2 served as a passivation layer and dopant source for the Fe_2O_3 photoanodes, which boosted their photocurrent by suppressing the substrate/hematite interfacial charge

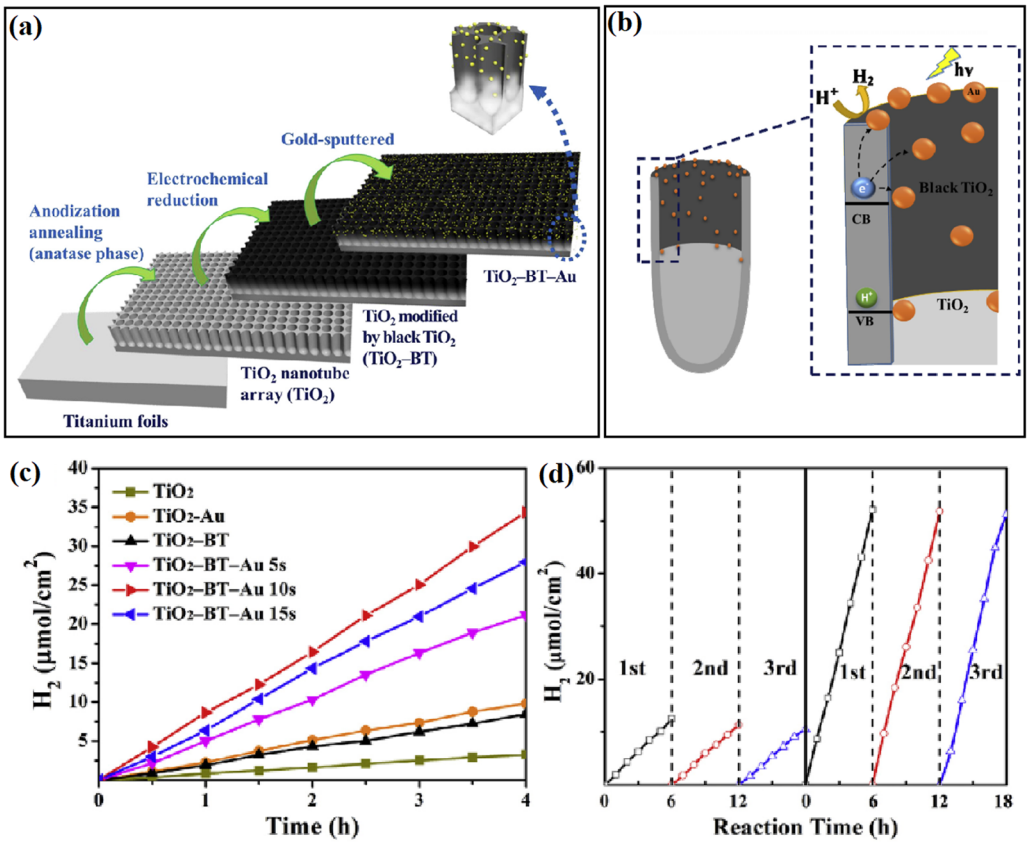

Fig. 4 (a) Method for the synthesis of TiO_2-BT-Au, (b) proposed mechanism of photocatalytic hydrogen evolution on TiO_2-BT-Au 10s, (c) H_2 evolution rates of different catalysts, and (d) cycle test of photocatalytic H_2 evolution over TiO_2 and TiO_2-BT-Au 10s. Reproduced with permission from ref. 51. Copyright 2018, Elsevier.

recombination and increasing the electrical conductivity by enabling the incorporation of Ti^{4+} (Fig. 6).

To date, deposition methods have been adopted by many researchers to obtain a passivation layer. However, it should be noted that the passivation layers did not have the same effects in all cases, where the performance of the deposited passivation layers depends on many experimental variables, such as the deposition condition, the thickness and crystallinity of the deposition layer.

3.3 Chemical bonding modification method

In addition to the introduction of a coating layer, the construction of chemical bonding to release stress or regulate the charge distribution is also an emerging passivation method. Chemical bonding can be introduced in the host material by ion doping,[60] plasma treatment,[61] high-temperature heating,[62–64] and solvent volatilization method.[65] The application of these methods will be introduced in the next chapter.

3.4 Other methods

Obviously, the realization of passivation engineering is not limited to the above-mentioned methods. In some reports, some special fabrication methods have also been adopted. For example, Liu *et al.*[66] inserted an ultrathin Al_2O_3 passivation layer between TiO_2 and NiOOH through a dipping method, followed by heating treatment (Fig. 7a). Kim[67] decorated conformal titanyl phosphate with a thickness of *ca.* 5 nm on the surface of TiO_2 using a sol–gel process. Liu *et al.*[68] fabricated a grey rutile TiO_2 passivation layer using a two-step calcination method. Nan *et al.*[63] treated a CdS@ZnO heterostructure using a calcining technique, where the heating treatment was found to efficiently improve the interface connection and crystallinity of the semiconductors (Fig. 7b–e). At the same time, the injection of electrons from CdS to ZnO could be improved with an increase in the heating temperature (Fig. 7f). The further measurement found that a $Cd_{0.8}Zn_{0.2}S$ buffer layer was formed between ZnO and CdS during the heating process, which efficiently released the interfacial stress, and thus paved a smooth pathway for the transfer of photogenerated charge carriers (Fig. 7g).

Table 1 lists most of the reported methods for the construction of a passivation layer with a comparison of their merits and shortcomings and their corresponding applicable systems.

4. Characterization of passivation engineering

The characterization of the passivation technique is an important task for evaluating its influence in photocatalysis. Also, to

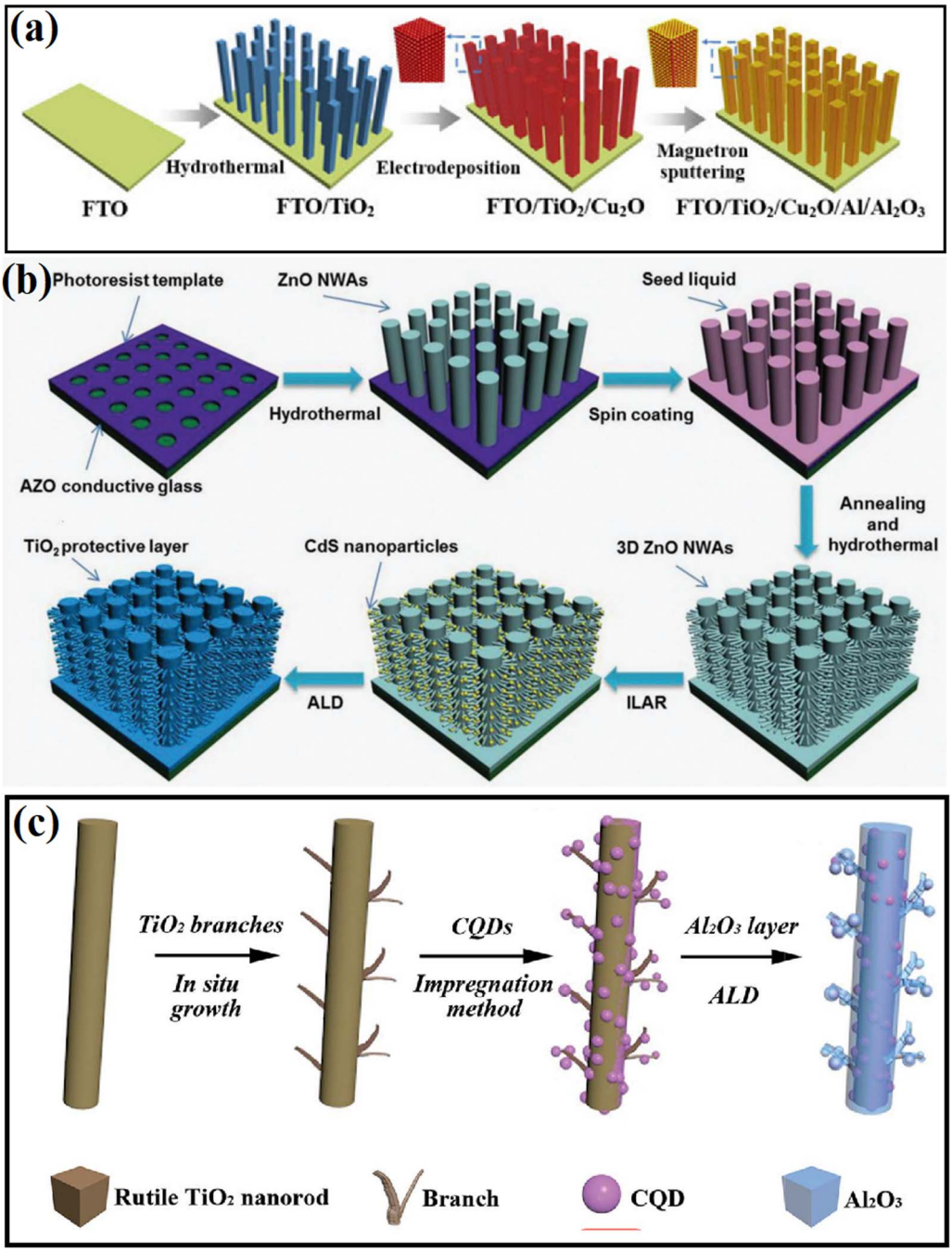

Fig. 5 (a) Schematic diagram of the preparation process of the $TiO_2/Cu_2O/Al/Al_2O_3$ photoanode. Reproduced with permission from ref. 52. Copyright 2020, Science Press. (b) Schematic diagram of the processes for the fabrication of 3D ZnO NWA-CdS. Reproduced with permission from ref. 55. Copyright, 2016 Wiley. (c) Preparation of CQDs/3D-TiO_2 NRs with a 5 nm Al_2O_3 layer. Reproduced with permission from ref. 56. Copyright 2018, The Royal Society of Chemistry.

establish guidelines for passivation engineering in PHE, it is necessary to accurately identify the passivation action, control the passivation degree and correctly evaluate the passivation effect, and thus establish the structure–activity relationship between passivation action and catalyst performance. To date, various characterization methods have been reported for characterizing the passivation effect in photocatalytic systems. Herein, we classify the existing techniques into microscopic characterization and spectroscopic characterization.

4.1 Microscopy characterization

4.1.1 Atomic-resolution spherical aberration-corrected transmission electron microscopy and transmission electron microscopy. Microscopy techniques are some of the most widely methods in giving a insights into the passivation engineering, in which the surface and structure change of photocatalysts can be observed directly. Atomic-resolution spherical aberration-corrected transmission electron microscopy (ACTEM) and

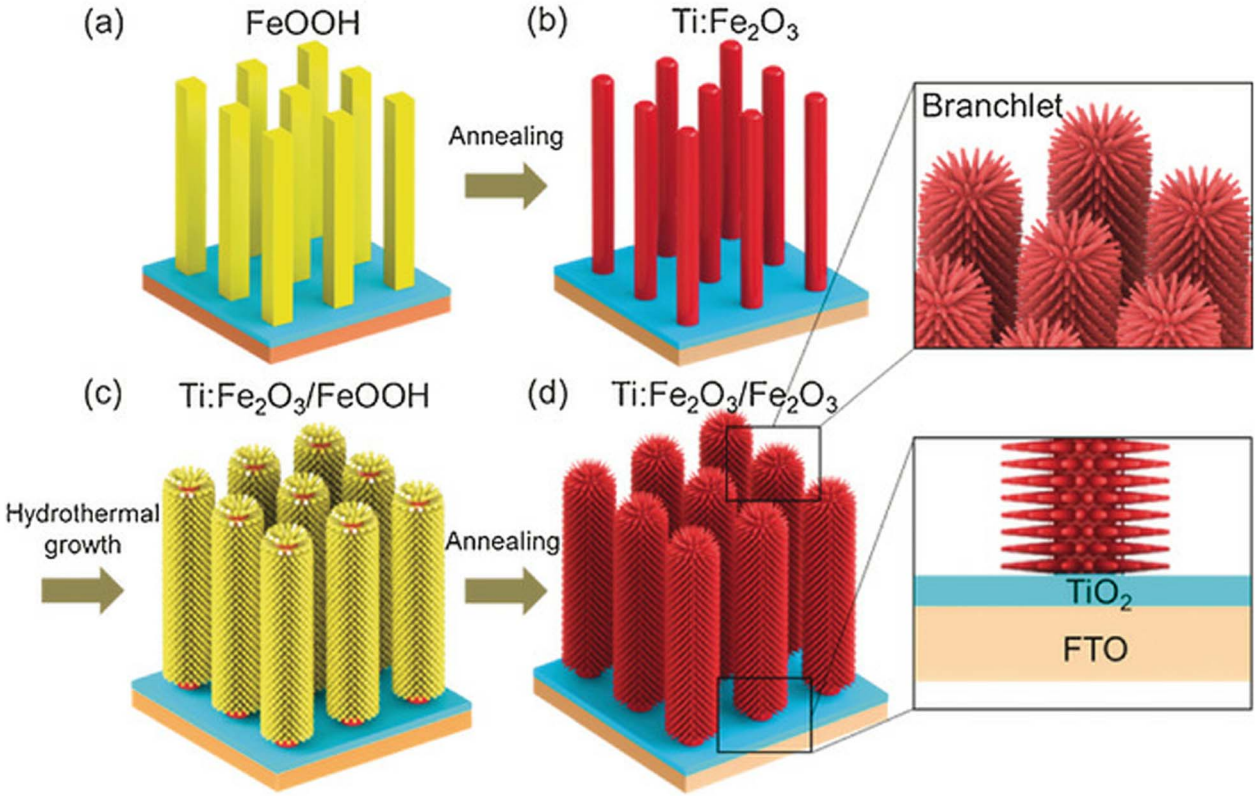

Fig. 6 Synthesis of TiO_2/Ti:Fe_2O_3 BNRs. Reproduced with permission from ref. 59. Copyright 2020, MDPI.

transmission electron microscopy (TEM) are important tools for characterizing the introduction of a surface passivation layer or intermediate passivation layer on a microscopic scale. By using these tools, we can deeply explore the effect of a passivation layer on the atomic arrangement at the surface/interface of catalyst. Fig. 8 exhibits some TEM and ACTEM images of the photocatalysts before and after passivation modification, in which the distinguished changes in transmission contrast, morphology and size of the samples can be found. In the case of ACTEM, the interfacial atomic arrangement can be clearly observed on the nanoscale.

4.1.2 Atomic force microscopy. Atomic force microscopy (AFM) is another important tool for characterizing the passivation effects on the microscopic scale. In general, the introduction of a surface passivation layer can result in a slight increase in the size of the sample, such as an increase in the diameter of nanoparticles or an increase in the thickness of two-dimensional materials. Fig. 9 presents some results from AFM characterization in the passivation field.

4.2 Spectral characterization

4.2.1 Electron paramagnetic resonance spectroscopy. Electron paramagnetic resonance (EPR) spectroscopy is a method for sensitively detecting vacancy-type defects in semiconductor photocatalysts.[59,81,82] By using this technology, researchers can obtain valuable fingerprint information about unpaired electrons and evaluate the type and relative concentrations of defects conceptually according to the different g values and signal intensities, thus further understanding the effect of passivation engineering on the defect state in catalysts.[81,82] It worth mentioning that given only a few paramagnetic species lead to interpretable EPR spectra, this method is more popular in the study of complex materials. For example, in a PDA-modified CdS system,[83] a significantly reduced EPR intensity of CdS could be observed for the sample with a thin passivation film of PDA, indicating that the PDA passivation layer efficiently eliminated the surface vacancy defects in CdS. Similarly, through EPR measurement, Liu *et al.*[59] found that rutile phase TiO_2 displayed an obvious EPR peak at $g = 1.997$, while no EPR peak at the same position was observed for heat-treated TiO_2, indicating that the oxygen vacancies were refilled by oxygen atoms and Ti^{3+} was mainly present under the formed surface passivation layer during the long calcination treatment in an air atmosphere. Wu *et al.*[84] carried out EPR measurements to reveal the effect of Fe on the photocatalytic process of TiO_2. As shown in Fig. 10, by detecting the active intermediates $^{\bullet}O_2^-$, $^{\bullet}OH$ and h^+, they found that the introduction of Fe contributed the most to the generation of $^{\bullet}O_2^-$ and $^{\bullet}OH$ during the photocatalytic reaction. Based on the experiments, they claimed that the passivation layer on the surface of Fe^0 was activated, and thus formed a Z-scheme heterojunction for high efficiency photocatalytic reaction.

4.2.2 X-ray photoelectron spectroscopy. XPS is a sensitive tool to characterize the surface chemical element composition and chemical state of photocatalysts. The interaction between

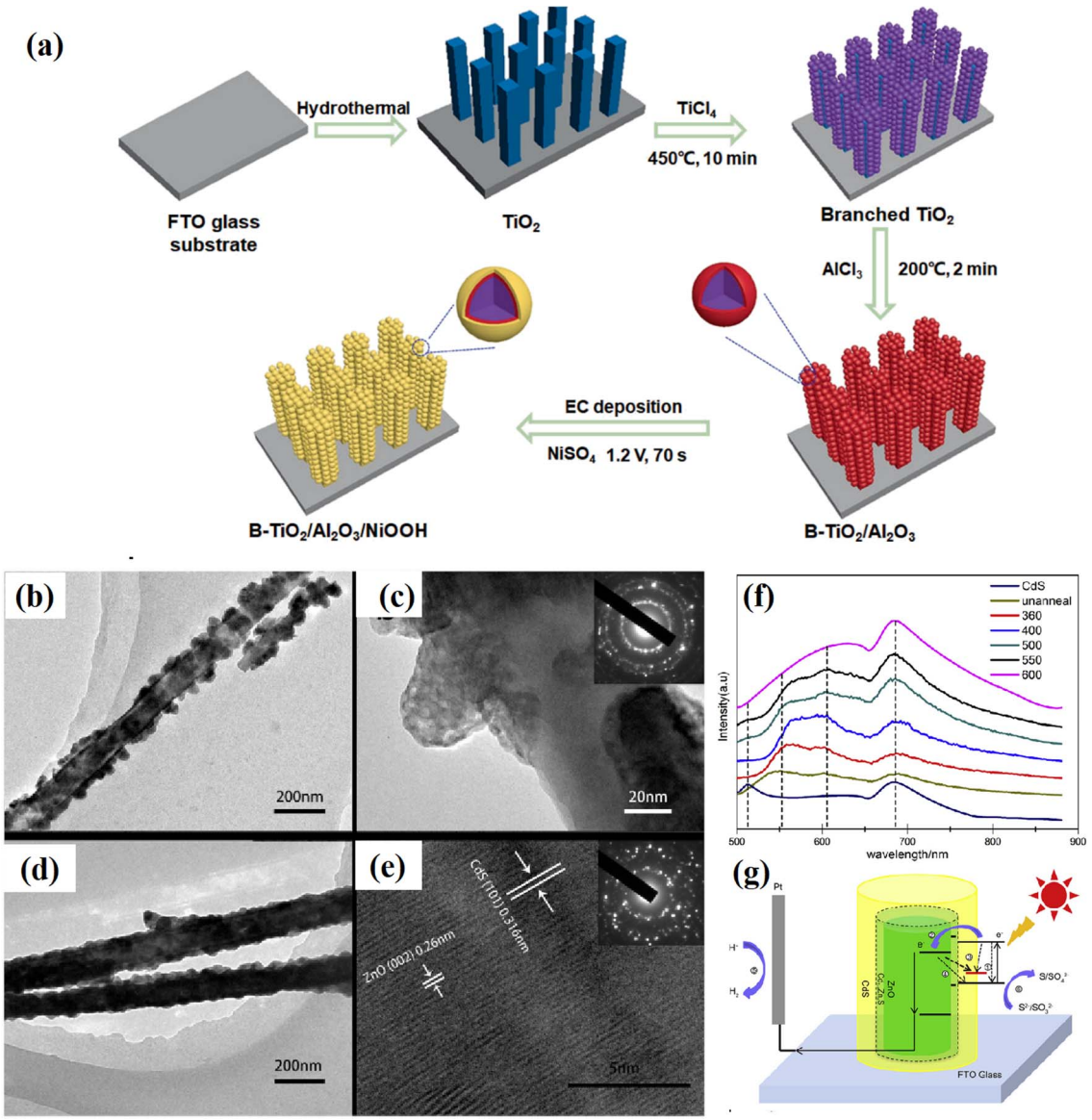

Fig. 7 (a) Procedure for the synthesis of the B-TiO_2/Al_2O_3/NiOOH photoanode, (b and c) TEM images of as-prepared and (d and e) calcined CdS/ZnO shell/core nanoarrays, (f) PL peaks of the CdS plane film and CdS/ZnO shell/core arrays calcined at different temperatures, and (g) schematic diagram of the PEC reaction mechanism on CdS/ZnO. Reproduced with permission from ref. 63. Copyright 2017, Elsevier.

semiconductors or on the surface of photocatalysts caused by a passivation layer, impurity ions or chemical bonding will alter the bonding energies or result in the formation of a new XPS signal, which provides convincing evidence for revealing changes in the interaction between objects caused by passivation engineering.[61,62,65–67,81]

Different from EPR, XPS can be widely applied for all types of inorganic and organic materials, as well as metals and semiconductors. The binding energy of different elements is closely related to the electron cloud density, thus reflecting the local change in chemical state and the interaction between different materials. In Yan's work,[62] XPS spectra were measured to understand the effect of a carbon passivation layer on the interaction between SnO_2 and g-C_3N_4. The binding energy of O–C in the pristine SnO_2/g-C_3N_4 was lower than that in SnO_2@C/CN-2, while the binding energy of π excitation in N 1s increased when a carbon layer was inserted in SnO_2/g-C_3N_4, indicating that the strong interaction among carbon, SnO_2 and g-C_3N_4 efficiently changed the electron density of the C and N atoms. Zhang *et al.*[61] carried out XPS measurement to evaluate the effect of N treatment on the carrier accumulation capability of the MoS_2/GaN heterostructure. As shown in Fig. 11a, before N treatment, the energy difference between Mo $3d_{5/2}$ and Ga $2p_{3/2}$ was 887.83 eV, while it increased to 888.36 eV after the N treatment, with a significant red-shift in the binding energy of Mo $3d_{5/2}$ towards a lower binding energy, indicating the enhanced accumulation of electrons on the surface of GaN. Xiao and coworkers[65] found that the surface deposition of K^+ resulted in an increased binding energy

Table 1 Comparison of the features of the commonly utilized methods in passivation engineering and their corresponding applicable systems

Fabrication method	Example	Advantage	Disadvantage	Applicable systems
In situ reaction method	Hydrothermal, solvothermal, wet-chemical sulfidation, photoreduction, hydrolysis, photo-deposition	Easy to operate, low cost	Difficult to accurately control the composition and content, limited passivation materials	Solid solution passivation layer, endogenous passivation layer, interfacial chemical bonding
Deposition method	Atomic layer deposition (ALD), chemical vapor deposition (CVD)	Controllable crystallinity, high purity and thinner layer	Time consuming, high cost	Exogenous passivation layer, interfacial layer
Chemical bonding modification method	Thermal polymerization, calcination	Easy to operate, low cost	Difficulty to accurately control, undefined mechanism	Ionic passivation layer
Electrochemical method	Electrostatic self-assemble, electrochemically anodization	Easy to operate, low cost, fine control to the passivation layer	Limited passivation materials	Exogenous passivation layer, interfacial layer
Other method	Plasma treatment, air oxidation, sol–gel	Easy to operate, low cost	Difficulty to accurately control	Exogenous passivation layer, surface layer

value of Ti 2p in KHB-TiO_2, and thus confirmed that K^+ can reduce the electron cloud density around Ti^{3+} and heal the defects in TiO_2 through the passivation effect (Fig. 11b). By using XPS measurement, Kim[67] observed the formation of a Ti–O–P bond and a slightly shifted XPS signal in H_3PO_4-passivated TiO_2 (Fig. 11c), indicating the strong interaction between TiO_2 and H_3PO_4.

4.2.3 X-ray absorption fine structure spectroscopy. Synchrotron radiation-based X-ray absorption fine structure (XAFS) spectroscopy is one of the most important and sensitive tools for examining the local atomic arrangement and electronic structures of materials, which provides even more precise information than that of XPS.[85–87] Through XAFS detection, the bonding types, oxidation states, bond angle, bond length, as well as the atomic coordination number of the detected atoms can be determined. All these outstanding detection abilities make the XAFS tool undoubtedly suitable for studying structural disorder, probing atomic defects and detecting other structural information. For example, Yang *et al.*[85] studied the effect of O doping on the chemical environment of $ZnIn_2S_4$ by using XAFS. As shown in Fig. 12, the Zn K-edge oscillation curve of the O-doped ZIS nanosheets shows both the signal of Zn–O coordination and the Zn–S coordination, providing strong evidence for the substitution of O atoms for S at the surface of ZIS. In addition, the disappearance of Zn–Zn coordination indicated that the introduction of O resulted in the structural distortion of ZIS. Zhao *et al.*[86] employed XAFS spectroscopy to detect the presence of defects in ZnAl-LDH nanosheets. In their work, a decrease in the Zn K-edge oscillation to about 2–10 $Å^{-1}$ was observed when the ZnAl-LDH bulk material changed to nanosheets, indicating the change in the coordinative environment around the Zn atoms. In addition, the shorter distance of the Zn–O bond in the ZnAl-LDH nanosheets clarified the occurrence of structural distortion in the formation of oxygen vacancies.

4.2.4 Raman spectroscopy. Raman spectroscopy reflects the change in chemical bonds, ground states vibration modes and lattice vibrational modes, which can be employed to study the structural characteristics of crystal materials.[41,61,82,84] The existence or elimination of defects and vacancies in photocatalysts can result in a change in their Raman shifts, create a new peak or decrease the intensity of their Raman signals. Accordingly, Raman spectroscopy can be utilized to reflect the effects of passivation engineering on the crystal structure and defect state of photocatalysts.[42,87–89] As shown in Fig. 13a, Alam and coworkers[89] deposited CdS on a C_3N_5 shell layer and studied the effect of C_3N_5 on the structure of CdS using Raman spectroscopy. Pure CdS displayed the typical 1LO and 2LO mode vibrations at 301 and 602 cm^{-1}, respectively. The intensity ratio of 2LO to 1LO reflects the exciton-phonon coupling strength, which is affected by the size, temperature, and laser excitation of the sample. A decline in the ratio was observed with the deposition of C_3N_5, indicating a decrease in phonon confinement caused by C_3N_5, which facilitated the reduction of the exciton-phonon coupling strength. In addition, Le *et al.*[42] observed a red-shifted Raman signal in AgO_x hole collector-modified $BiVO_4$, indicating an increase in the disorder of the V–O bonds within $BiVO_4$ caused by AgO_x.

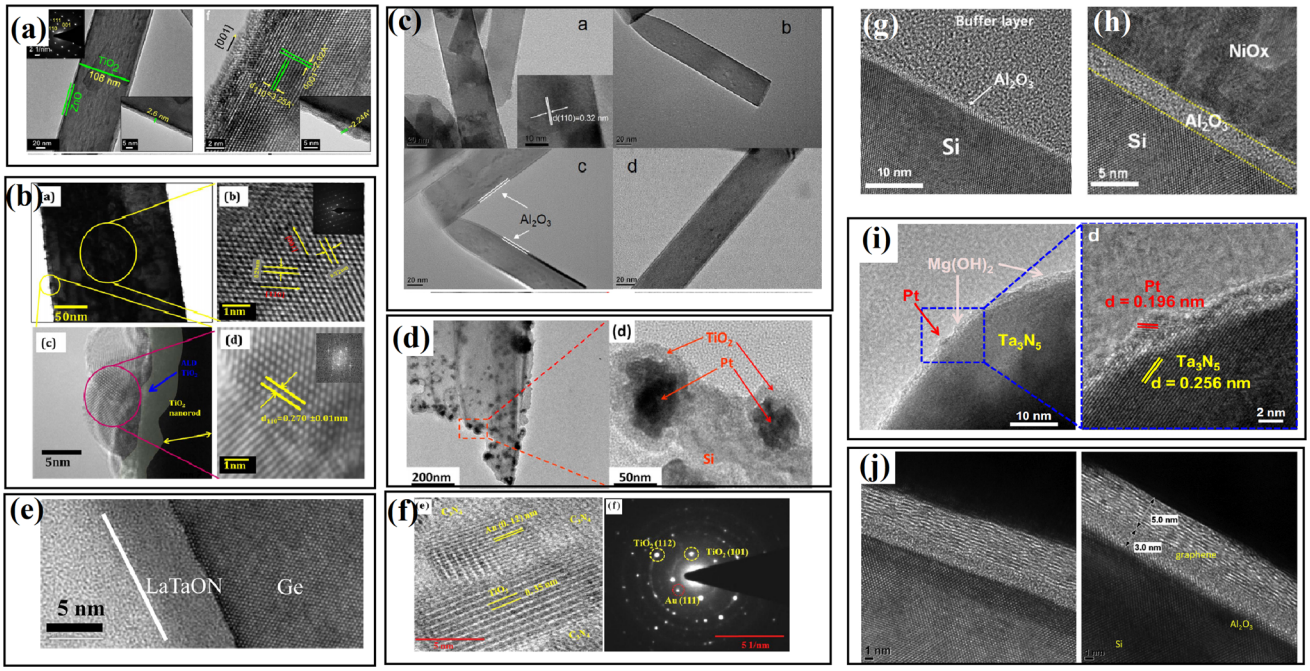

Fig. 8 Some TEM and ACTEM images of the passivation-modified samples reported in the literature.[68–76] (a) Reproduced with permission from ref. 68. Copyright 2016, Springer. (b) Reproduced with permission from ref. 69. Copyright 2015, the American Chemical Society. (c) Reproduced with permission from ref. 70. Copyright 2017, Bentham Science Publishers. (d) Reproduced with permission from ref. 71. Copyright 2015, the American Chemical Society. (e) Reproduced with permission from ref. 72. Copyright 2017, Elsevier. (f) Reproduced with permission from ref. 73, Copyright 2016 Elsevier. (g) and (h) Reproduced with permission from ref. 74. Copyright 2016, Elsevier. (i) Reproduced with permission from ref. 75. Copyright 2016, Academic Press Inc. (j) Reproduced with permission from ref. 76. Copyright 2018, Elsevier.

4.2.5 Photoluminescence spectroscopy. Photoluminescence spectroscopy is a direct tool for identifying the relaxation process of photogenerated electrons.[55,59,78] When high-energy electrons return from the excited energy state to a lower energy state, they usually release energy in the form of luminous radiation. In general, photoluminescence can be ascribed to the direct recombination of electrons and holes, as well as the defect-induced luminescence due to the capture of electrons in the trap levels. Based on this theory, the passivation of defect states in a catalyst can be confirmed by the detection of its photoluminescence spectra, in which the elimination of defect states usually results in the absence of defect emissions.

Nayak *et al.*[78] fabricated an NiFe-LDH/N-GO/g-C_3N_4 nanocomposite using N-doped rGO as a passivation layer. In the PL spectrum, the introduction of N-rGO efficiently decreased the emission caused by the recombination of photogenerated charge carriers, indicating the suppressed charge recombination. In addition, two obvious PL peaks corresponding to the defect region and oxygen vacancies could be seen with different emission intensities with a changed in the amount of introduced passivation layer, indicating the importance of an appropriate passivation layer in manipulating the amount of defects and vacancies. Neuderth and coworkers[90] studied the effect of a passivation layer on InGaN by using PL spectroscopy, as shown in Fig. 14b–d. The deposition of Al_2O_3 resulted in a significant increase in the PL intensity of the substrate, while a decrease in the PL intensity was obtained in the TiO_2 deposited sample. By contrast, CeO_2 barely displayed an effect on the PL of the substrate. This work demonstrated that PL spectroscopy is a direct tool reflecting the interaction between the passivation layer and the substrate.

In passivation engineering, spectroscopic techniques are mainly utilized for the qualitative analysis of defects or vacancies in the substrate materials. However, in actual research, different characterization methods are usually combined, and the different data support and assist each other, verifying the realization of passivation engineering from different perspectives and dimensions and revealing the impacts of passivation engineering on catalytic systems.

5. The categories and mechanism of passivation engineering in PHE

As mentioned, passivation engineering not only provides protection for the sensitive photocatalytic surface, but also inhibits the harmful inner charge recombination. As shown in Tables 2 and 3, passivation engineering can be divided into surface passivation and interfacial passivation according to the modification position. Based on our research, it was found that various materials, including metallic compounds, amorphous compounds, halogen, carbon, and graphene, have been utilized as a passivation layer, and different passivation mechanisms have been proposed by researchers in these systems. In the following paragraphs, we introduce the design and mechanism of these materials in passivation engineering in detail.

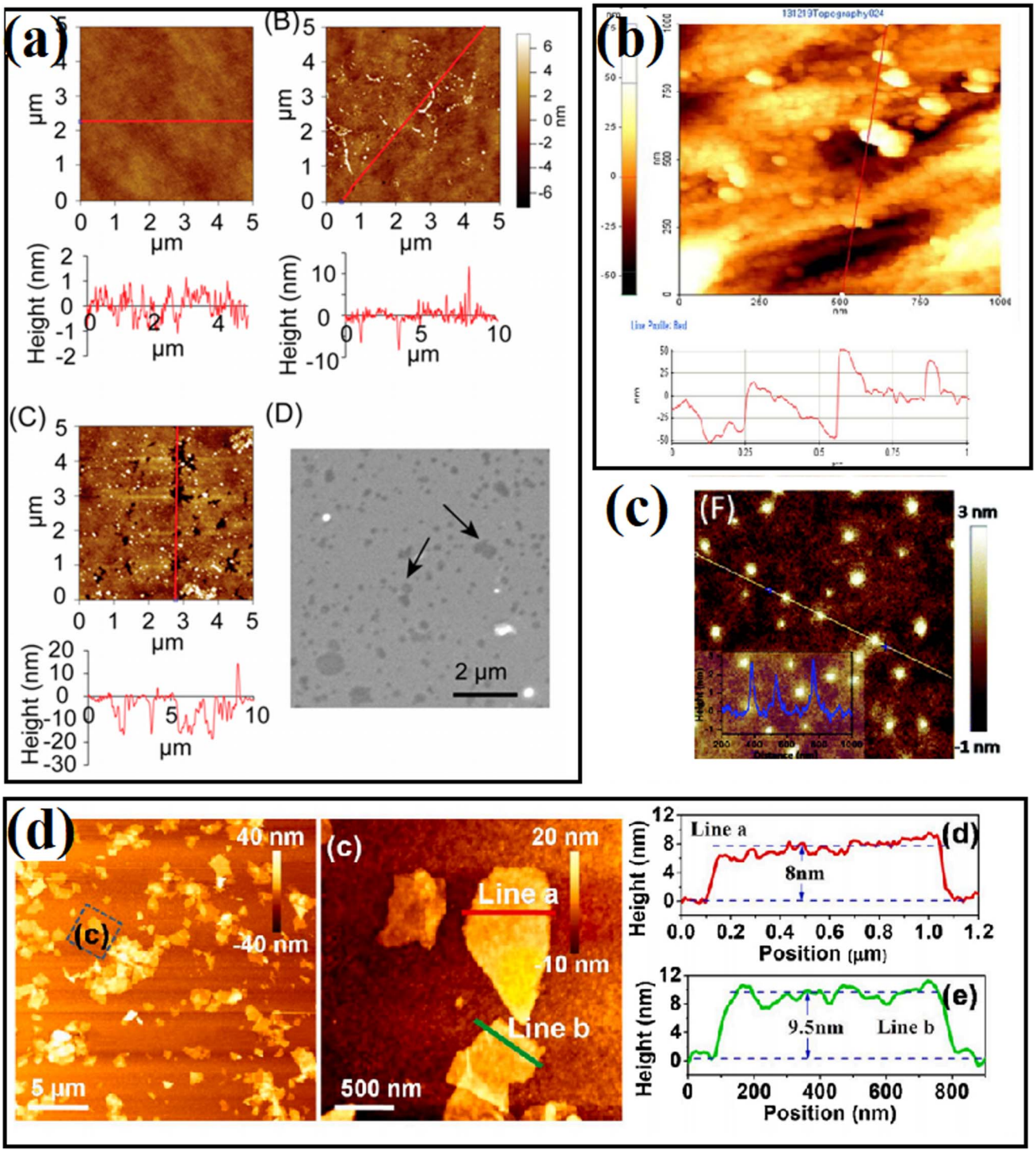

Fig. 9 AFM images in passivation engineering.[77–80] (a) Reproduced with permission from ref. 77. Copyright 2017, the American Chemical Society. (b) Reproduced with permission from ref. 78. Copyright 2019, Springer. (c) Reproduced with permission from ref. 79. Copyright 2020, MDPI. (d) Reproduced with permission from ref. 80. Copyright 2021, Elsevier.

5.1 Surface passivation

The surface of a catalyst is the most active position because of the accumulation of photogenerated electrons and holes, where the photogenerated electrons are consumed by protons (H^+) to generate hydrogen or consumed by a more competitive reductant, and the photogenerated holes easily trigger the oxidation reaction of the catalyst itself, thus resulting the deactivation of the catalyst. For example, the surface sulfide ions (S^{2-}) in metal sulfide-based photocatalysts are easily oxidized by photogenerated holes to form sulfate (SO_4^{2-}) and/or sulfur (S^0), resulting in their deactivation, and the Ag^+ in silver-

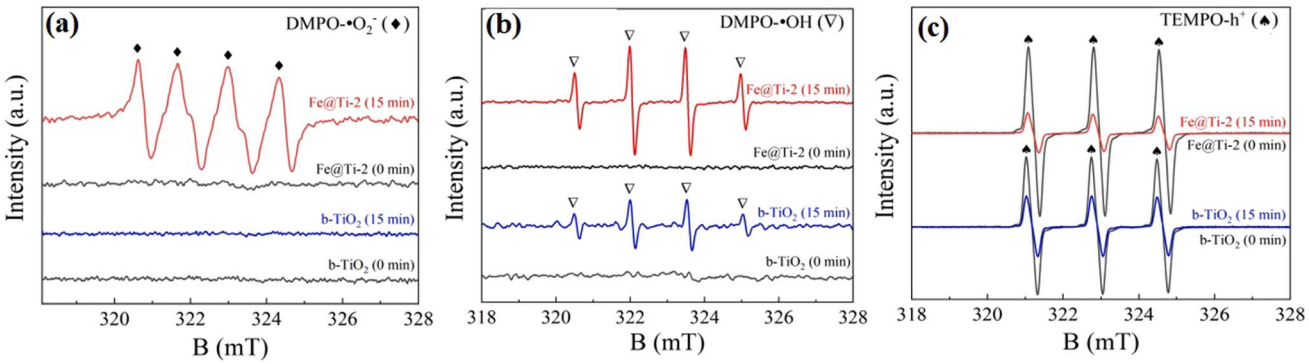

Fig. 10 EPR spectra of Fe@Ti-2 for (a) DMPO-$^{\bullet}O_2^-$, (b) DMPO-$^{\bullet}$OH and (c) TEMPO-h^+. Reproduced with permission from ref. 84. Copyright 2022, Elsevier.

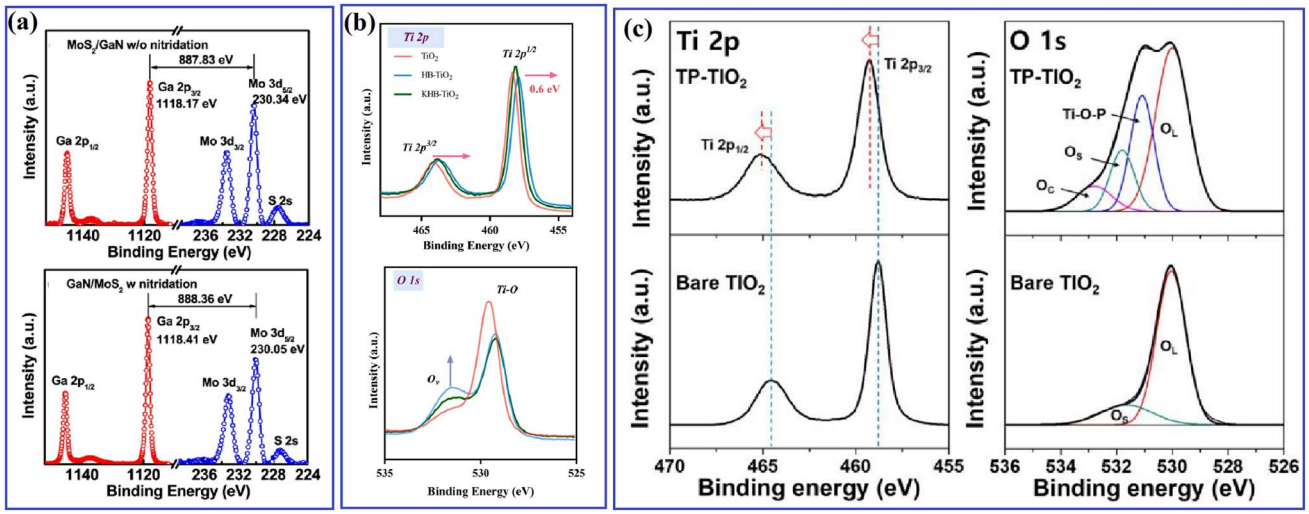

Fig. 11 (a) Ga 2p and Mo 3d core-level spectra obtained from the MoS_2/GaN interface without and with nitridation treatment. Reproduced with permission from ref. 61. Copyright 2018, the American Chemical Society. (b) Ti 2p and O 1s XPS spectra of TiO_2, HB-TiO_2 and KHB-TiO_2. Reproduced with permission from ref. 65. Copyright 2023, Elsevier. (c) Ti 2p and O 1s XPS spectra of bare TiO_2 and TP-TiO_2. Reproduced with permission from ref. 67. Copyright 2018, MDPI.

containing compounds can be reduced to Ag^0 by photo-generated electrons, leading to the decomposition of the compounds.[90,91]

5.1.1 Passivation by inert cover layer. From the perspective of passivation, by modification with some metal oxides such as TiO_2, CeO_2, and Al_2O_3, metal sulfides such as CdS and CoS_2,

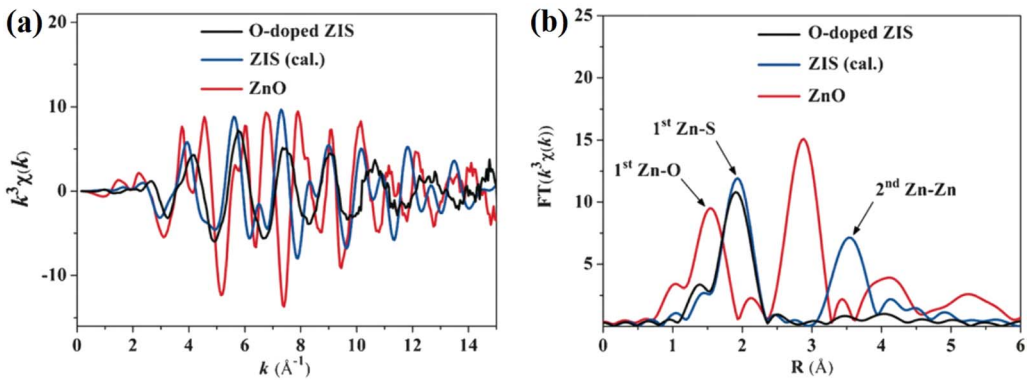

Fig. 12 (a) Zn K-edge extended EXAFS oscillation function and (b) corresponding Fourier transforms of the O-doped ZIS nanosheets, calculated ZIS and ZnO. Reproduced with permission from ref. 85. Copyright 2016, Wiley-VCH.

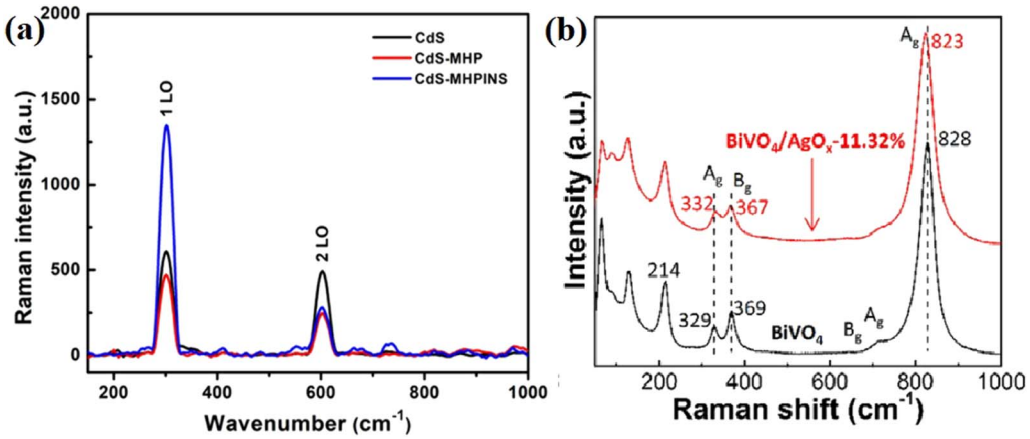

Fig. 13 (a) Raman spectra of the pristine CdS nanowire and heterojunctions of CdS with C_3N_5 nanosheets. Reproduced with permission from ref. 89. Copyright 2021, the American Chemical Society. (b) Raman spectra of bare $BiVO_4$ and $BiVO_4/AgO_x$-11.32% sample. Reproduced with permission from ref. 42. Copyright 2021, Elsevier.

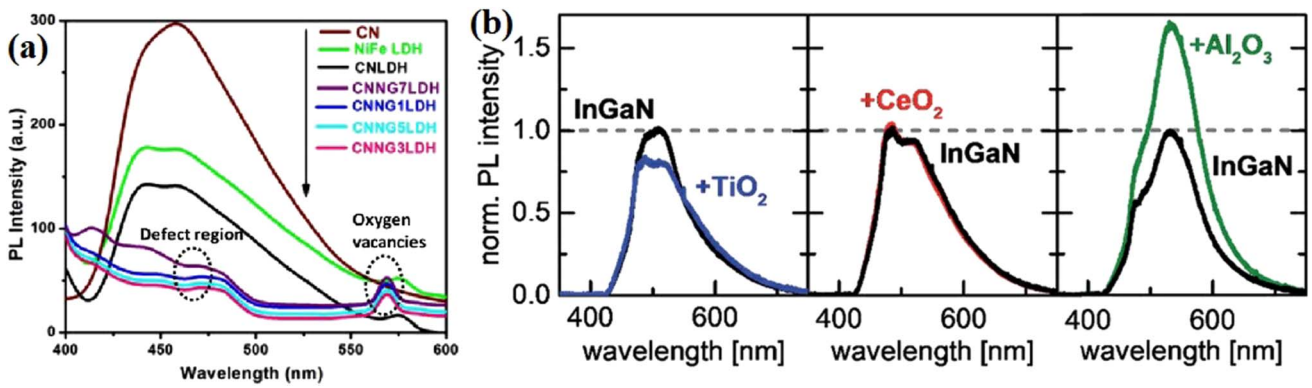

Fig. 14 (a) PL spectra of NiFe LDH, CN, CNLDH and CNNGxLDH measured at the excitation energy of 380 nm. Reproduced with permission from ref. 78. Copyright 2019, Nature. (b) PL spectra of TiO_2-, CeO_2- and Al_2O_3-coated InGaN nanowires. Reproduced with permission from ref. 90. Copyright 2018, The Royal Society of Chemistry.

special ions such as potassium and chloride, *etc.*, susceptible photocatalysts can be isolated from the liquid environment and/or the surface traps/defects, which are easy to induce photogenerated carrier recombination, can be eliminated, thus suppressing the adverse surface reactions.[91–95] For example, Kim and coworkers[91] deposited an ultrathin TiO_2 layer on the surface of ZnO/MnO_2 hybrids using the atomic layer deposition method (Fig. 15a and b), where the ultrathin layer of TiO_2 was efficient in preventing the direct contact between ZnO and the electrolyte, ultimately reducing photo-corrosion. In addition, the deposition of the TiO_2 layer could reduce the tunneling barrier and interfacial resistance, which is beneficial for the rapid transfer of charge carriers. As a result, the TiO_2-coated sample displayed much higher activity and stability than the ZnO/MnO_2 catalyst (Fig. 15c and d). As shown in Fig. 15e and f, the deposition of TiO_2 improved the surface charge separation and enhanced water oxidation during the PEC process. In addition, it also provided holes at the solid–liquid interface, reduced the photo-corrosion of ZnO/MnO_2, acted as a charge-storage zone, and ultimately injected the photogenerated holes into the electrolyte.

Rasamani *et al.*[92] passivated Pt-tipped CdSe nanorods using an epitaxially grown atomic-level CdS layer to efficiently eliminate the surface defects/trap states in the CdSe nanorods. It was found that after the treatment, the sample displayed 6.5 times higher H_2 evolution ability. Besides, the formation of strong chemical boding on the surface of bare catalysts has also been proven to be an efficient way to decrease the adverse surface charge recombination by eliminating the surface states. In 2015, Kim[67] modified TiO_2 photocatalysts with a titanyl phosphate passivation layer, where the phosphate anions were strongly bound on the surface Ti atoms with oxygen bridges, inducing the formation of Ti–O–P–O bonds, which resulted in a reduction in the trap states originating from the Ti^{3+} defects. The decoration of the passivation layer enabled a long-term photochemical performance with the enhanced photocatalytic activities of TiO_2. Chen *et al.*[93] deposited an integrated cobalt disulfide passivation layer on Si microwires, where the covering

Table 2 Summary of the literature on passivation engineering with the details of passivation materials, fabrication methods, passivation types and passivation mechanisms (in the column "type", the symbols "SP" and "IP" represent "surface passivation" and "interfacial passivation" respectively)

Catalyst	Passivation material	Fabrication	Type	Mechanism	Ref.
$ZnO/MnO_2/TiO_2$	TiO_2	ALD	SP	Protecting substrate from photo-corrosion	91
$Pt/TiO_2/InAs/p\text{-}Si$	TiO_2	ALD	SP	Protecting the vulnerable InAs	33
$SiP/TiO_2/Al_2O_3$	Al_2O_3	ALD	SP	Providing fixed charge to promote the separation and transport of electrons and holes	96
TiO_2-CdTe/Fe_2O_3	TiO_2	Calcination	SP	Addressing the excessive surface defects and the slow carrier transfer	114
$TiO_2/Cu_2O/Al/Al_2O_3$	Al_2O_3	Air oxidation	SP	Protecting vulnerable substrate	52
$BiVO_4/AgO_x$	AgO_x	Calcination	SP	Quenching the photogenerated holes to stabilize $BiVO_4$	42
VO-B/N-ZGO	B and N doping	Calcination	SP	Proving efficient charge compensation by B–N bond formation	115
C-Cu-CdS	Carbon	Solvothermal	SP	Protecting vulnerable substrate	116
Al_2O_3-CQDs/TiO_2	Al_2O_3	ALD	SP	Restraining electrons from being captured by surface trap states through fixed negative charge	56
$TiO_2/Ti/Si$	TiO_2	Sputtering	SP	Protecting Si from surface passivation	53
CdSe/CdS	CdS	Oil bath	SP	Decreasing the surface-deep trap states of CdSe, inducing tunnel effect	101
C@SiNW/TiO_2	Carbon	Calcination	SP	Protecting the Si from oxidation	34
Cu-TiO_2@C	Carbon	Thermal reduction	SP	Providing a chemical protection to the coated Cu nanoparticle	95
KHB-TiO_2	K^+	Calcination	SP	Healing the electronic structure of the TiO_2 surface	65
TiO_2@Si	TiO_2	ALD	SP	Protecting silicon from photo-oxidation	117
$Fe_2O_{3@}Fe^0$@black-TiO_2	Fe_2O_3	Air oxidation	SP	Protecting Fe^0 from oxidation	118
CdSe-Cl	Cl	Water bath	SP	Decreasing electron trap states on the surface of CdSe	103
TiO_2/conformal titanyl phosphate	Conformal titanyl phosphate	Sol–gel	SP	Promoting the production and stabilization of hydroxyl radicals on the surface of TiO_2	67
CoS_2-Si	CoS_2	Photolithography and dry etching	SP	Preventing Si from oxidation	94
CdSe/CdS/Pt	CdS	Hydrothermal	SP	Eliminating surface traps	93
$In_xGa_{1-x}N$/GaN/ultra-thin oxides	TiO_2, CeO_2 and Al_2O_3	ALD	SP	Eliminating surface states	90
$Zn_{1-x}Cd_xS$/NiO	NiO	Photodeposition	SP	Inhibiting substrate from photocorrosion	119
Cu-doped $AgIn_5S_8$/ZnS	ZnS	Solvothermal	SP	Passivating surface defects and enhancing photogenerated charge transportation	120
Cu_2ZnSnS_4/CdS/TiO_2	TiO_2	Hydrolysis	SP	Inhibiting substrate from photocorrosion	98
SnO_2@C/CN	Carbon	Calcination	IP	Stabilizing small size semiconductors; inducing the formation of strong internal electric field	62
CdS/CdZnS/ZnO	CdZnS	Calcination	IP	Decreasing the interface stress by minimizing lattice mismatch	63
TiO_2-BT-Au	Black TiO_2	Electrochemical anodization	IP	Electronic storage and prevention of hole recombination	51
NiFe-LDH/N-rGO/g-C_3N_4	N-rGO	Electrostatic self-assembly	IP	Providing bridge for the combination of different 2D nanolayers, enhancing interfacial charge interactions	78
CdS@Al_2O_3@CdS	Al_2O_3	ALD	IP	Decreasing interfacing stress and facilitating charge transfer through fixed negative charge	57
Cu/Cu_2S/ZnS	Cu_2S	Wet-chemical sulfidation	IP	Increasing interfacial charge transfer and changing the Helmholtz layer potential drop	49
CoNi-C_3N_4/CdS	Co–S bonding	Photoreduction method	IP	Accelerating electron transfer through Co–S bonds	32
P-C_3N_4/Ni	P–Ni bonding	Thermal polymerization	IP	Bridging incompatible C_3N_4 and Ni through N–P–Ni bonding	60
B-TiO_2/Al_2O_3/NiOOH	Al_2O_3	ALD	IP	Reducing the surface defects of TiO_2 and benefiting the extraction of holes to the surface	66
MoS_2/GaN	N_2	Plasma treatment	IP	Facilitating electron accumulation capability through N_2-induced conduction band offset	61
g-C_3N_4/GO/BiOI	GO	Oil bath	IP	Forming close energy band to enhance electron transfer from g-C_3N_4 to BiOI	107

Table 3 Summary of the utilized materials in different passivation modes and the basic passivation mechanism of different systems

Passivation mode		Materials	Mechanism
Surface passivation	Metallic compound	SiO_2, Al_2O_3	Providing the substrate from photo-corrosion
		TiO_2	Improving the surface charge separation
		$Ti_3(PO_4)_4$, CdS, CoS_2	Reducing surface defect states through the formation of chemical bonding
		ZnO, CeO_2	Reducing the tunneling barrier and interfacial resistance
		Al_2O_3, MnO_2, Cr_2O_3, TiO_2	Inhibiting the photocatalytic active materials from inactivating oxidation
	Ionic passivation layer	K^+, Cl^-, other halogen ions	Healing surface defect and balancing the density of free electrons
Interfacial passivation	Amorphous compounds	Al_2O_3, TiO_2	Releasing interface stress, increasing charge tunneling ability
		GO, rGO	Decreasing the band barrier and interface resistance between the directly contacted semiconductors
		Carbon	Stabilizing small size semiconductors; inducing the formation of strong internal electric field
	Solid solution	S_x–In–P_{1-x}, CdZnS	Decreasing the interface stress by minimizing lattice mismatch
	Interfacial chemical bonding	Ni–P–N, Co–S bonds	Bridging incompatible semiconductors; forming atomic level electron transfer channel
	Impurity atoms	N, Nd, C	Manipulating the energy band structure, increasing charge carriers generation speed and decreasing recombination losses

CoS_2 layer resulted in the formation of a fluffy surface (Fig. 16a–d) and dramatically improved the photocatalytic stability and activity of Si (Fig. 16e and f). It was found that the CoS_2-Si hybrids displayed lower charge transfer resistance among the photo-absorber, co-catalyst, and redox couples due to the decoration of CoS_2 (Fig. 16g–i). At the same time, the XANES spectra revealed that more vacancies were present in the unoccupied S-3p states of the CoS_2-Si-250 electrode, which indicated that the CoS_2-Si electrode presented a lower negative charge of S_2^{2-} and formed a weaker S–H_{ads} bond strength to promote the water splitting efficiency. Furthermore, the deposited CoS_2 layer protected Si from directly exposure in liquid, and thus working worked as a passivation layer to defend Si from oxidation, which efficiently improved the stability of the sample.

Another widely utilized strategy is protecting the vulnerable surface by using a stable chemical layer, such as Al_2O_3 and TiO_2. Feng *et al.*[56] anchored an Al_2O_3 ultra-thin layer on the surface of CQDs/TiO_2 using the atomic layer deposition method, and it was found that the introduction of Al_2O_3 significantly improved

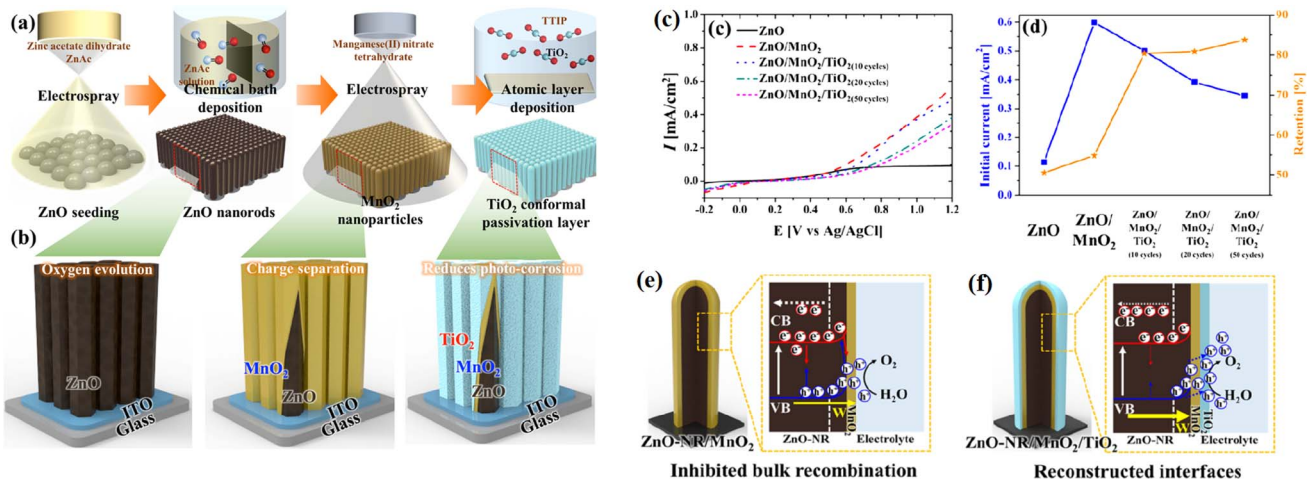

Fig. 15 (a) Schematic of the fabrication of ZnO/MnO_2/TiO_2 nanorods, (b) illustration of the effect of each coated layer, (c) and (d) are respectively photocurrent density and stability of the samples, and effects of (e) MnO_2 in promoting charge separation and (f) TiO_2 as a passivation layer. Reproduced with permission from ref. 91. Copyright 2020, Elsevier.

the IPCE value and photoconversion efficiency of the sample (Fig. 17). However, a crucial factor that needs to be considered is the thickness of the passivation layer. A too thick passivation layer may result in a decline in photocatalytic performance due to the quickly developed adverse factors, resulting in the loss of light harvest ability, charge transfer ability, and the limited exposure of active sites. In this study, it was found that the sample behavior was obvious correlated with the thickness of the deposited Al_2O_3 layer. Consequently, it was found that 5 nm is the best parameter for Al_2O_3 coating. Alternatively, a too thin coating layer could not passivate the trapping state effectively. Further, a too thick coating prevented the photogenerated electrons and holes from migrating to the surface of the nanorods by transiting the Al_2O_3 layer due to its large band gap. The effect of the Al_2O_3 layer in the system is shown in Fig. 17d, where negative charges exist between the Al_2O_3 layer coated using the ALD technique and the photocatalyst surface. The surface band bending induced by the electron depletion on the surface of the photocatalyst restrains the photogenerated electrons from being captured by the surface trap states, and thus isolates the photoinduced charges in space, reduces their recombination rate and suppresses the back reaction effectively.

In addition to photo-corrosion, another factor playing a role in the deactivation of catalysts is self-passivation, which means that some active components in the catalyst are converted into new substances that do not have catalytic activity during the catalytic reaction. For example, Si has one of the best band gaps and band alignments as the photocathode of a two-photo-absorber water-splitting device, but one of the major limitations of silicon is that it is easily oxidized to SiO_2, which does not have catalytic activity. Also, Cu photocatalysts can only be kept in an oxygen-free environment because Cu nanoparticles are easy oxidized by oxygen, which limits the applications and studies using Cu catalysts. An exciting idea is that the surface passivation strategy can be utilized to inhibit the passivation of some active components themselves to extend the lifetime of catalysts. The typical cover layers reported include Al_2O_3, MnO_2,

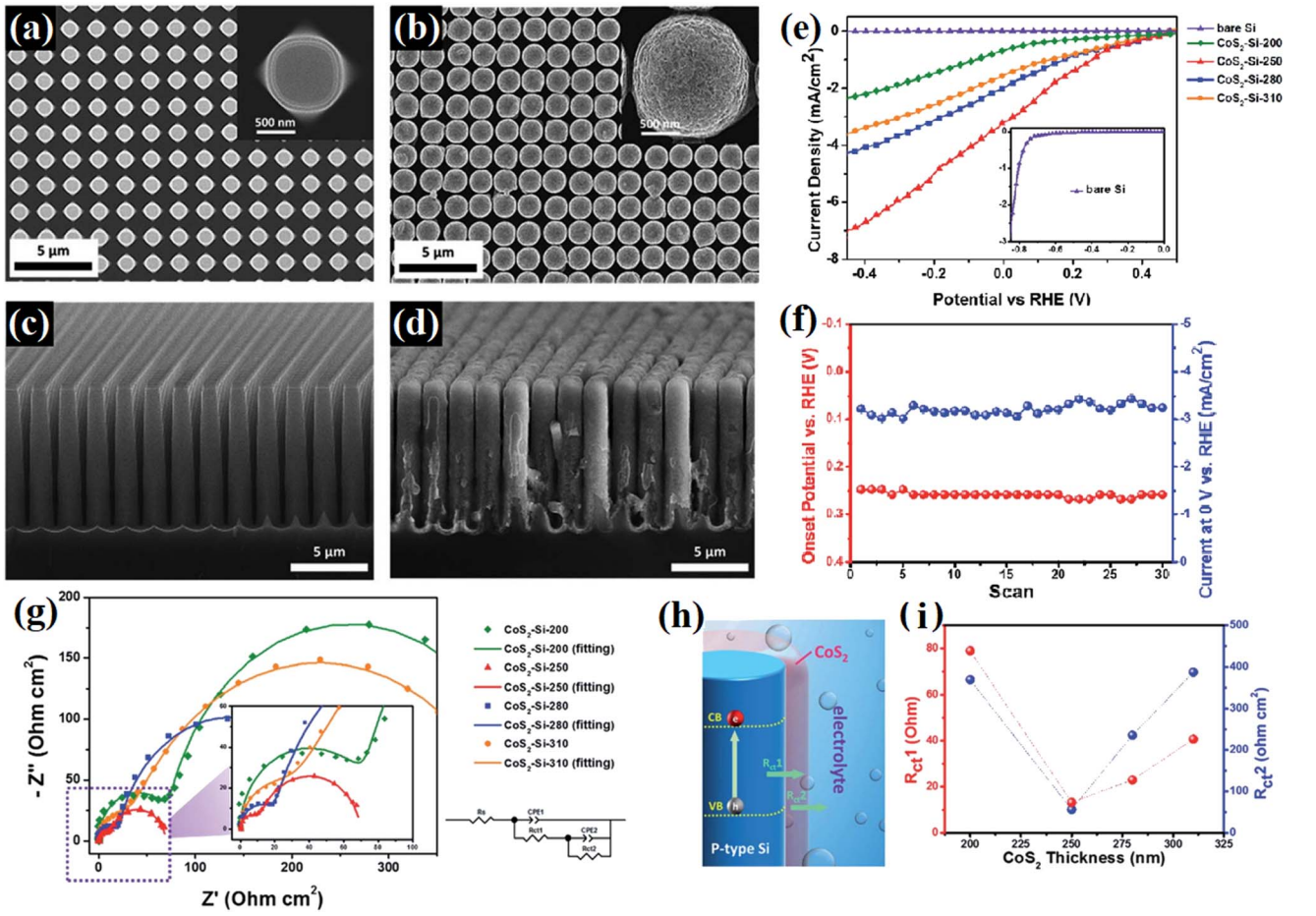

Fig. 16 (a and b) Top view and (c and d) cross-sectional SEM images of bare Si and CoS_2-Si-250 microwire arrays. (e) Linear-sweep voltammograms of CoS_2-Si electrodes with various CoS_2 thicknesses, (f) onset potential and photocurrent of the CoS_2-Si electrode *versus* the number of scans, and (g) electrochemical impedance spectra of CoS_2-Si electrodes at 0.4 V bias under solar illumination. (h) Schematic illustration of charge transfer resistance between the composition materials of the photoelectrode (R_{ct_1}) and between the photoelectrode and redox couples in the electrolyte (R_{ct_2}). (i) Charge transfer resistance *versus* CoS_2 thickness of CoS_2-Si electrodes. Reproduced with permission from ref. 93. Copyright 2015, the Royal Society of Chemistry.

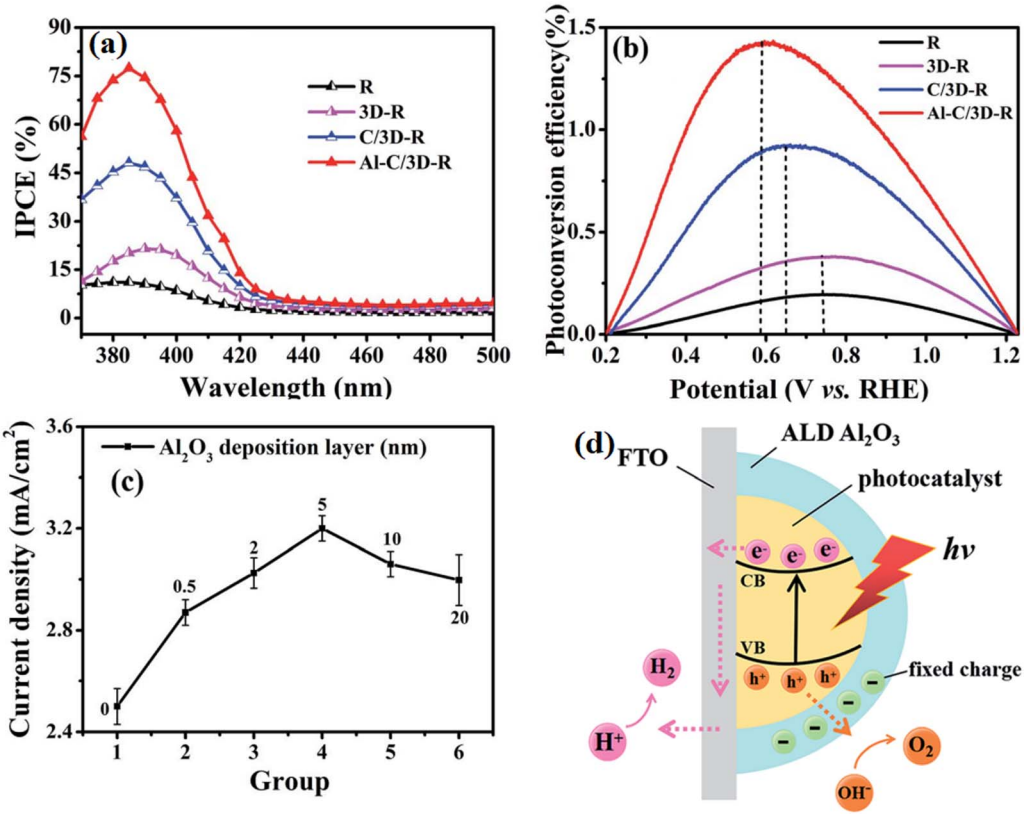

Fig. 17 (a) IPCE spectra and (b) calculated solar-to-hydrogen (STH) efficiencies of the samples. (c) Line chart measured at 1.23 V *vs.* RHE of thickness of Al_2O_3 layer. (d) Mechanism model for the role of Al_2O_3 coating in the separation of electron–hole pairs. Reproduced with permission from ref. 56. Copyright 2018, the Royal Society of Chemistry.

Cr_2O_3, and TiO_2.[87,88,91–96] For example, Seger *et al.*[53] deposited a sputtered 100 nm TiO_2 layer on top of a thin Ti metal layer, which was found to be efficient in protecting the Si photocathode from oxidation during photocatalytic H_2 evolution. Chen and coworkers[94] covered a Cu-TiO_2 nanocomposite using a carbon protection layer without changing the basic morphology and structure of the substrate catalyst. Cu-TiO_2@C could effectively adsorb hydroxyl radicals, improving the electron transfer speed between TiO_2 and Cu nanoparticles, thereby greatly improving the photocatalytic activity of TiO_2 (Fig. 18). In addition, the carbon layer could provide a chemical protection to the Cu nanoparticles and increase the stability of the photocatalysts.

Besides, Al_2O_3 was also utilized as a cover layer to passivate the inner catalyst from rapid charge recombination due to its special fixed negative charge. By using the ALD method, Zhang *et al.*[95] deposited Al_2O_3 on the surface of an SiP QDs/TiO_2 NR heterostructure and obtained significantly enhanced hydrogen evolution ability over the catalyst. As shown in Fig. 19a, a TiO_2 nanorod (NRs) array was firstly grown on FTO glass through the hydrothermal method, and subsequently they deposited SiP quantum dots (QDs) on the TiO_2 NR array to form SP QD/TNR composites using a continuous dip coating approach. Subsequently, a thin Al_2O_3 layer was coated on the surface using the ALD method. The morphology and element distribution of the sample can be observed on right of Fig. 19a. The experimental results indicated that the introduction of an Al_2O_3 layer obviously improved the photoconversion efficiency of the sample (Fig. 19b and c). In addition, it was found that the photoelectric behavior of the sample varied with the thickness of the Al_2O_3 layer, an Al_2O_3 layer with a thickness of about 3 nm resulted in the highest current density (Fig. 19d and e). When the thickness of Al_2O_3 was less than 3 nm, the Al_2O_3 layer was too thin to effectively passivate the surface state of SiP/TiO_2 and prevent photo-corrosion, whereas a too thick Al_2O_3 layer prevented the absorption of light and the transmission of photogenerated charge carriers to the surface of the catalyst due to its large bandgap, as shown in Fig. 19f.

Surface passivation is the external manifestation of multiple complex effects in the cover layer. Qiu *et al.*[96] studied the effect of a surface TiO_2 passivation layer on the PHE ability of GaAs, and found that the TiO_2 layer hosted active surface states on GaAs, which increased the recombination rate of photogenerated electron–hole pairs. At the same time, the introduced TiO_2 layer dramatically decreased the potential barrier for photocatalytic reactions, and this benefit outweighed the unfavorable effects of charge recombination and resulted in an enhancement in the photocurrent density. In addition, they demonstrated that the thickness of the TiO_2 layer also has an obvious effect on the sample. The highest PHE efficiency was obtained with the loading of a 1 nm TiO_2 passivation layer, while no improvement was observed in the 10 nm TiO_2-

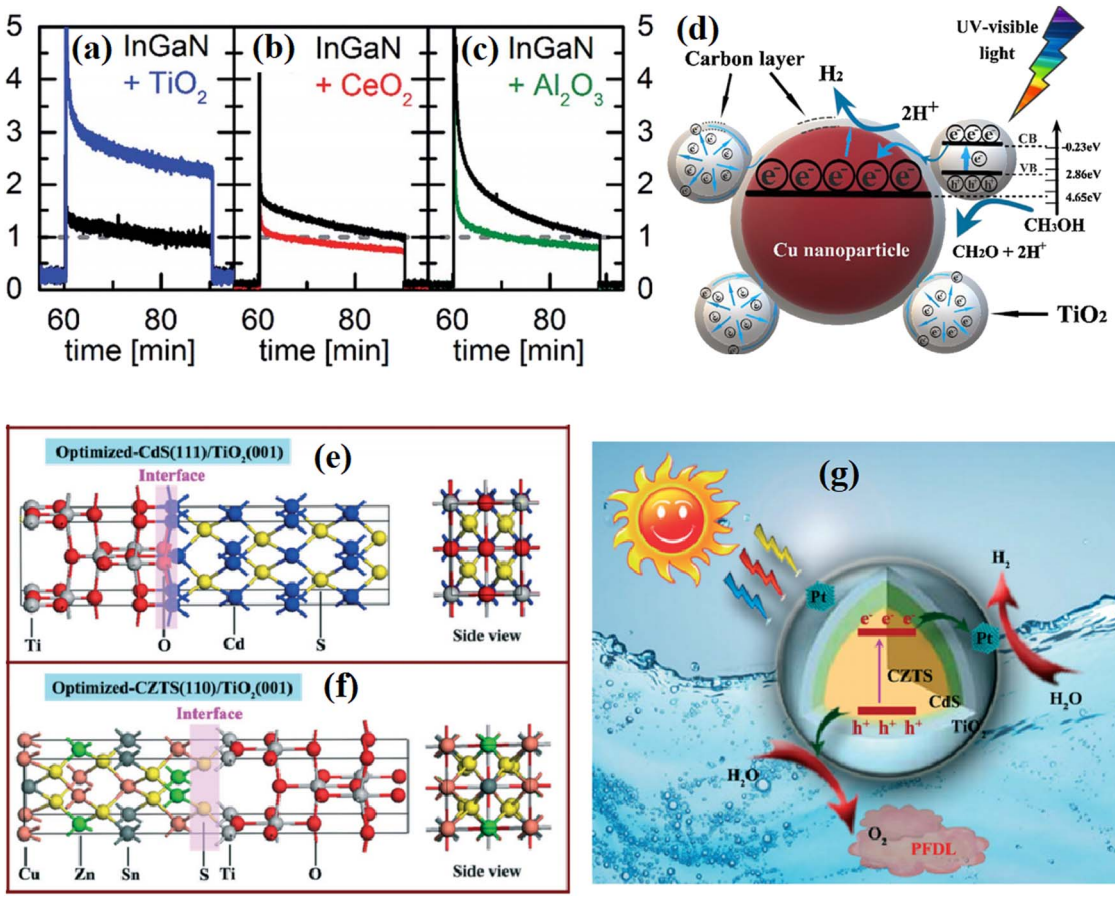

Fig. 18 (a–c) Influence of different ALD coatings on the PC of InGaN/GaN NWs: PC measurements of TiO_2-, CeO_2- and Al_2O_3-coated NWs. Reproduced with permission from ref. 90. Copyright 2018, Elsevier. (d) Influence of different ALD coatings on the PC of InGaN/GaN NWs: PC measurements of TiO_2-, CeO_2- and Al_2O_3-coated NWs. Reproduced with permission from ref. 94. Copyright 2019, Elsevier. (e) and (f) Optimized interfaces of CdS(111)-TiO_2(001) and CZTS(001)-TiO_2(001), respectively. (g) Mechanism of overall water splitting over the CZTS/CdS/TiO_2/Pt double-heterojunction photocatalyst with PFDL assistance under visible illumination. Reproduced with permission from ref. 94. Copyright 2022, Elsevier.

decorated sample, which is because the insulating nature of TiO_2 eventually outweighed its benefits. Neuderth *et al.*[90] studied the surface passivation effect of ultra-thin TiO_2, CeO_2 and Al_2O_3 coatings on the photoelectrochemical performance of $In_xGa_{1-x}N$/GaN nanowires, and found that the best passivation of surface states resulted in an increase in the anodic photocurrent by a factor of 2.5 with the deposition of 5 nm TiO_2. By contrast, the covering of CeO_2 and Al_2O_3 resulted in a decrease in the photocurrent (Fig. 18a–c), which is because the high band energy offset of Al_2O_3 to InGaN suppressed the transfer of photocarriers and resulted in enhanced radiative recombination, while the increased defect recombination brought by CeO_2 aggravated the carrier losses. Zhang *et al.*[97] investigated the role of TiO_2 on the surface of Cu_2ZnSnS_4/CdS hybrids. Based on theoretical calculation, they claimed that the formation of Cd–O and Ti–S covalent bonds between TiO_2 and CdS is crucial in achieving a well-matched interface architecture between the photocatalyst and the chemically inert TiO_2 protective layer (Fig. 18e–g), which restrained the photo-corrosion of the catalyst induced by the formed nascent O_2 and remarkably enhanced the catalyst stability during photocatalytic water splitting. Yu *et al.*[98] studied the origin of enhanced PHE activity in g-C_3N_4/TiO_2 through DFT calculations, and they claimed that the different modifications on TiO_2 surface will greatly affect the distribution of electrons and holes at the heterojunction interface, where oxygen vacancy and hydrogen passivation showed a more significant influence on the g-C_3N_4/A001 interface and induced more significant charge separation.

By using Au-tipped CdS nanorods as a model, Ben-Shahar *et al.*[99] studied the effects of different surface passivation layers on the photocatalytic function of hybrid nanoparticles. They found that the surface coating affected the trapping of photogenerated charge carriers at the surface defects, thus changing the photocatalytic efficiency. The apparent quantum yield (AQY) of the photocatalysts strongly depended on the surface passivation layer, where the lowest AQY was observed for thiolated alkyl ligands, while the best photocatalytic activity was found for the PEI-coated sample (Fig. 20a). The corresponding measurements indicate that the improved H_2 evolution activity is correlated with the effect of passivation of the surface traps. As shown in Fig. 20b and c, a faster bleach recovery was observed for the PEI-coated hybrid nanoparticles, which means

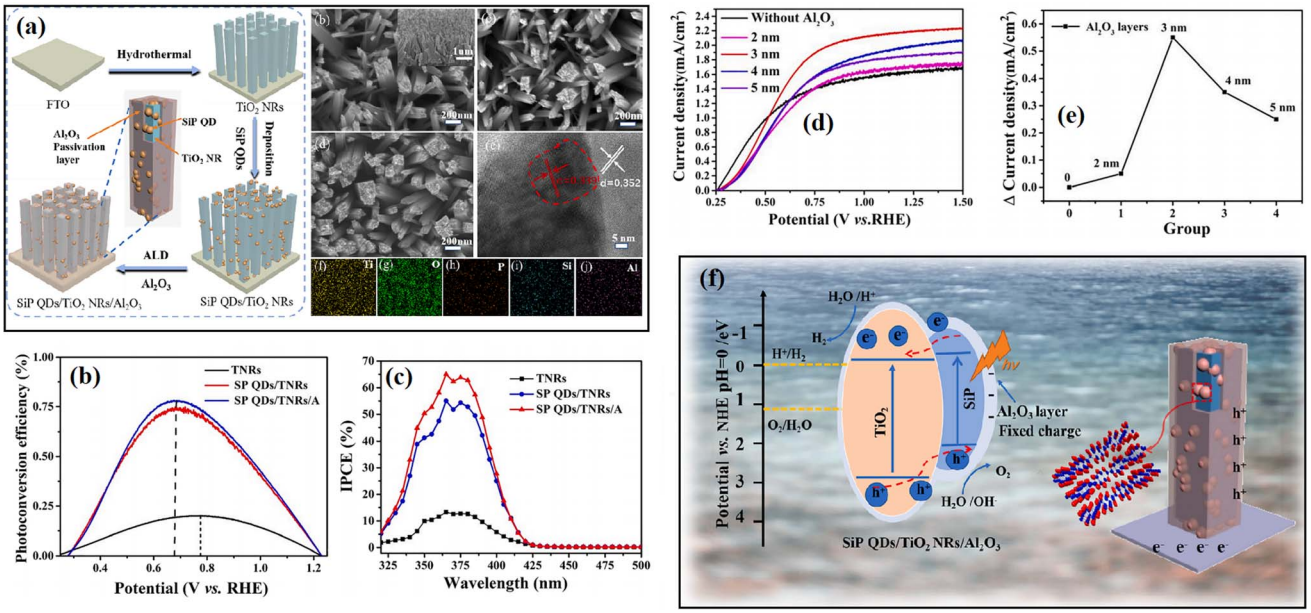

Fig. 19 (a) Schematic of the synthesis of SiP QDs/TiO_2 NRs/Al_2O_3 and the morphology of the sample. (b) Calculated solar-to-hydrogen (STH) efficiencies and (c) IPCE spectra of the samples. (d) LSV curves and (e) corresponding line charts measured at 1.23 V *vs.* RHE of SiP QDs/TiO_2 NRs/Al_2O_3 with different dipping times in SiP QD solution. (f) Schematic of the nanostructure and charge separation and transfer mechanism of the sample. Reproduced with permission from ref. 95. Copyright 2022, Elsevier.

faster and more efficient charge separation. This work demonstrated that different coatings affect the surface passivation efficiency in trapping the charge carriers.

Besides, the harmful trap states created by the intrinsic defects in some semiconductors can also be passivated by covering a protection layer.[100] In 2011, Thibert and co-workers[101] found that the coverage of a CdS shell efficiently enhanced the H_2 evolution ability of CdSe quantum dots (DSs), while CdSe itself was completely inactive in pure water (Fig. 21a). Broad-band transient absorption spectroscopy was performed to reveal the defect states in the catalyst. As shown in Fig. 21b, an obvious emission peak arose from the recombination of deeply trapped charge carriers at 700 nm in CdSe QDs but absent in CdSe/CdS, indicating that the CdS shell passivated the deep traps caused by the defects in CdSe. Based on the broad-band transient absorption spectroscopy measurements, the authors proposed that the surface-deep trap states with energies lying below the reduction potential necessary for H_2O reduction were passivated by the CdS shell, thus efficiently facilitating the utilization of photogenerated charge carriers and boosting the H_2 generation (Fig. 21c and d). In addition, Tongying *et al.*[102] investigated the lifetime of photogenerated charge carriers in CdS and the CdSe/CdS system by using femtosecond transient differential absorption (TDA) spectroscopy, and found that the coverage of CdS efficiently prolonged the lifetime of electrons and suppressed the harmful recombination caused by trap states. Moreover, the CdS shell provided electrons to the CdSe core and formed a type I energy transfer mechanism. The combination of defect passivation and the supplementary of additional carriers from the CdS shell significantly improved the H_2 generation rate of bare CdSe.

Inhibiting the easily inactivated photocatalyst surface by using a chemical inert covering layer is efficient in prolonging the working lifetime of photocatalysts, but this process is often at the cost of reducing their catalytic activity. Thus, to minimize the adverse influence of the coating layer on the catalytic activity, some key points should be considered in the selection and design of the coating layer, as follows: (1) the covering layer should have good electrical conductivity or proper thickness to minimize its effect on the migration of photogenerated charge carriers. (2) The introduction of a coating layer should not affect the light absorption performance of the substrate catalyst. (3) The coating layer should have good interfacial compatibility or the ability to form chemical bonds with the substrate catalyst, thus avoiding the generation of new defects. (4) Suitable energy band arrangement is also an important factor to minimize the loss of catalytic activity.

5.1.2 Self-modified surface passivation. Besides the deposition of an external passivation layer, some self-modification strategies have also been used to passivate the harmful charge recombination and improve the PHE kinetics of materials. Xiao *et al.*[65] modified Pt/TiO_2 with a K^+ passivation layer and constructed a two-electron migration photocatalytic system. The realization of accurate passivation depends on the targeted selection of the raw materials and well-designed preparation process. As shown in Fig. 22a, the crucial factor of the surface passivation engineering was the introduction of a K^+ passivation layer with defect-healing function. Through the participation of $NaBH_4$ and KBH_4, the O atoms on the surface of TiO_2 were partially substituted by H and B, and thus Ti–H bonds and Ti–B bonds were formed, which could subsequently be healed to Ti–O bonds in the air to construct defect-free TiO_2. The core

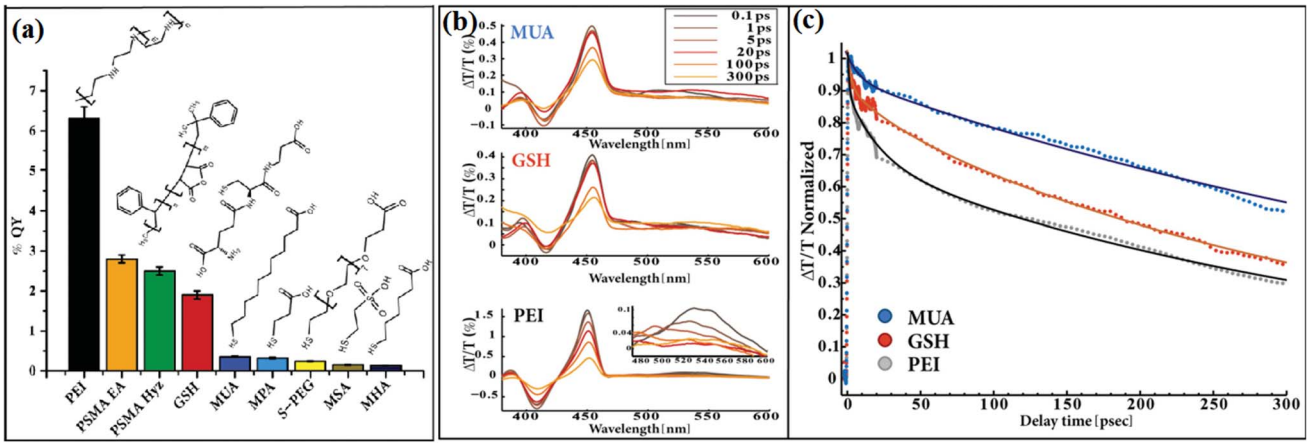

Fig. 20 (a) Apparent photocatalysis % QY values for a wide range of surface coatings, including thiolated alkyl ligands, GSH, and polymer coating. (b) Transient absorption spectra of CdS-Au HNPs for different surface coatings at 450 nm excitation. Expansion of the Au plasmon region for the PEI coating are presented in the inset (lower left frame). (c) Normalized transient absorption kinetics of the bleach recovery at 460 nm, corresponding to the first exciton transition of the CdS nanorod component, together with the exponential fits (continuous lines) for CdS-Au HNPs with different surface coatings. Reproduced with permission from ref. 99. Copyright 2015, Wiley.

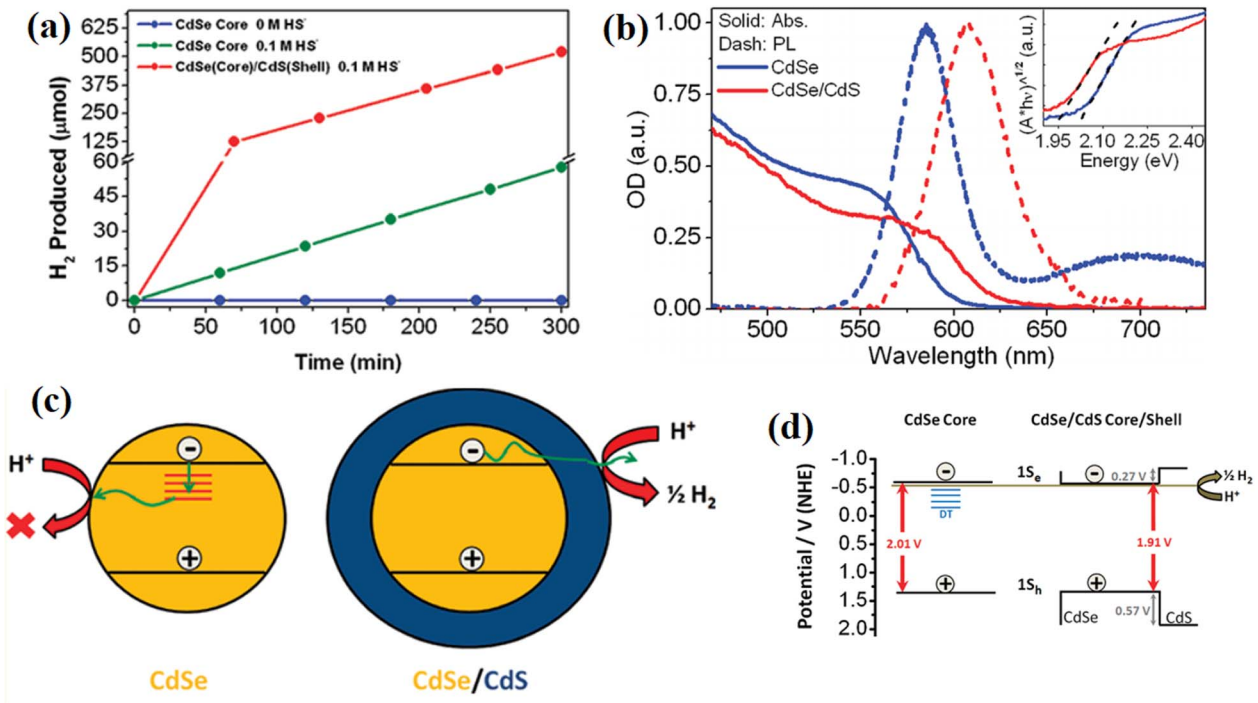

Fig. 21 (a) Photocatalytic hydrogen evolution for CdSe and CdSe/CdS QDs in pure H_2O and 0.1 M HS solution under visible light illumination from a 300 W Xe lamp equipped with a 400 nm long pass filter. (b) Static absorption (solid lines) and photoluminescence (dashed lines) spectra of CdSe (blue lines) and CdSe/CdS core/shell QDs (red lines). (c) and (d) Mechanisms of CdS in passivating the trap states of CdSe and facilitating H_2 evolution. Reproduced with permission from ref. 101. Copyright 2011, the American Chemical Society.

role of the K^+ passivation layer was to inhibit the increase in electron cloud density caused by B-doping engineering and balance the free electrons adsorbed by O_v (Fig. 22b). When a large number of two-electrons induced by O_v and B-doping engineering migrate to the KHB-TiO_2 surface, the stable electronic structure healed by the K^+ passivation layer will directly transfer the two-electrons to Pt and be used for photocatalytic hydrogen evolution, thus dramatically accelerating the evolution of hydrogen (Fig. 22c). Based on theoretic calculation (Fig. 22d), it was believed that K^+ mainly deposited in the vicinity of the B-doping sites and O_v, and the formed K–O_v–Ti and O–K–B–Ti chemical bonds are crucial in healing the surface electronic structure of TiO_2. As a result, the introduced K^+ played several roles in increasing the splitting of water, such as

balancing the free electrons generated by O_v, preventing the free electrons in the conduction band from participating in the carrier separation, and inhibiting the generation of holes induced by B-doping.

At the same time, Kim *et al.*[103] investigated the H_2 evolution ability of chlorine-passivated CdSe nanocrystals, and found that Cl passivation removed the electron trap states in the CdSe NCs and resulted in an increase in the photoluminescence quantum yield from 9% to 22% after Cl treatment. This is because the introduced ammonium chloride solution resulted in Cl-passivation of the surface dangling bonds, and thus inhibited the harmful consumption of electrons from the surface of CdSe (Fig. 23a and b). Moreover, by controlling the size of CdSe, they found that the photocatalysis was enhanced significantly in 4.5 nm CdSe NCs after the Cl treatment, whereas smaller CdSe NCs exhibited lower photocatalytic activity after Cl treatment. The different changing trends indicate that the Cl atoms passivate the surface trap states without altering the density of native organic ligands because both the conduction band edge and trap states in the small-size CdSe are above the water reduction potential (Fig. 23c and d).

Liu *et al.*[104] investigated the halogen edge passivation effect of antimonene nanoribbons on the H_2 evolution reaction with first-principles density functional theory calculations. It was found that both the armchair and zigzag structures of the antimonene nanoribbons can be relaxed to a more stable state by the halogen atom than the hydrogen atom-passivated ones due to the larger electronegativity and mass of the halogen atoms. In addition, it was also noticed that the passivation effect caused by the halogen endowed the catalysts with different band gaps. As a result, the tensile strain can promote the solar to hydrogen transfer efficiency. All the samples satisfied the REDOX potentials for H_2 evolution under tensile strain of greater than 4%, while the maximum value can reach the theoretical limit of 17.51% under the tensile strain of 12%.

Some self-modification strategies can also create an inert protection layer on unstable substrates. For example, Liu *et al.*[59] treated rutile TiO_2 using a two-step calcination method. A dense layer with a thickness of 2–5 nm was formed on the outermost layer of the rutile TiO_2, resulting in a change in color from white to gray (Fig. 24a and b). The EPR measurement reflected that a large amount of O vacancies were formed during the high-temperature treatment, which can improve the photogenerated carrier separation and transmission efficiency (Fig. 24c). The formed dense surface passivation layer efficiently hindered the further diffusion and infiltration of oxygen molecules into the interior oxygen vacancies, thus endowing the photocatalyst with an outstanding long-time reaction stability.

In total, the surface of photocatalysts can be passivated by using some ions or passivation layers, where the surface passivation of photocatalysts is essential not only for increasing their efficiency, but also for enhancing their resistance to corrosion and dissociation, which are caused by photogenerated intermediates.

5.2 Interfacial passivation

With the development of technology for the preparation and characterization of nanomaterials, the construction of heterostructure systems has been considered more promising in obtaining much improved H_2 evolution ability due to the formation of an inner electric field on the interface, which is effective in reducing the recombination of photogenerated electrons and holes. However, an inescapable fact is that the high separation of charge carriers at interface requires intimate contact and low mismatched interface between two semiconductors, which is difficult to precisely achieve because the difference in lattice parameters and crystal growth directions

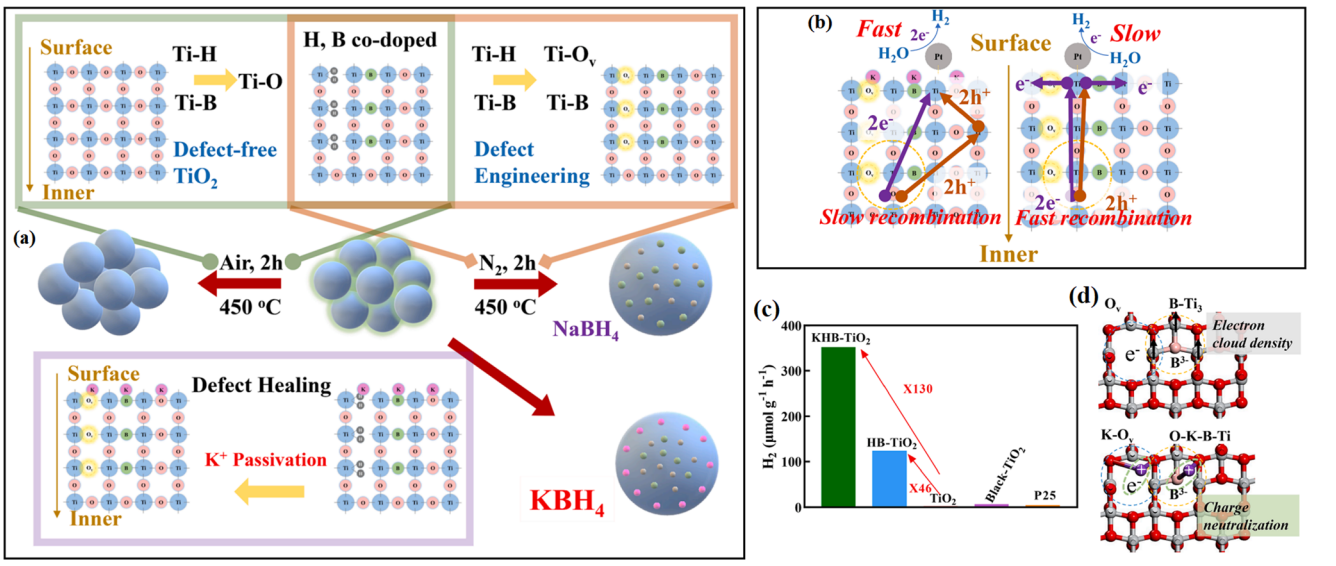

Fig. 22 (a) Strategies for the synthesis of TiO_2, HB-TiO_2, and KHB-TiO_2. (b) Photoelectron migration mechanism of KHB-TiO_2 and HB-TiO_2. (c) Hydrogen production efficiencies of different samples in 1 h. (d) Mechanism of K^+ healing the electronic structure of TiO_2 surface. Reproduced with permission from ref. 65. Copyright 2021, the American Chemical Society.

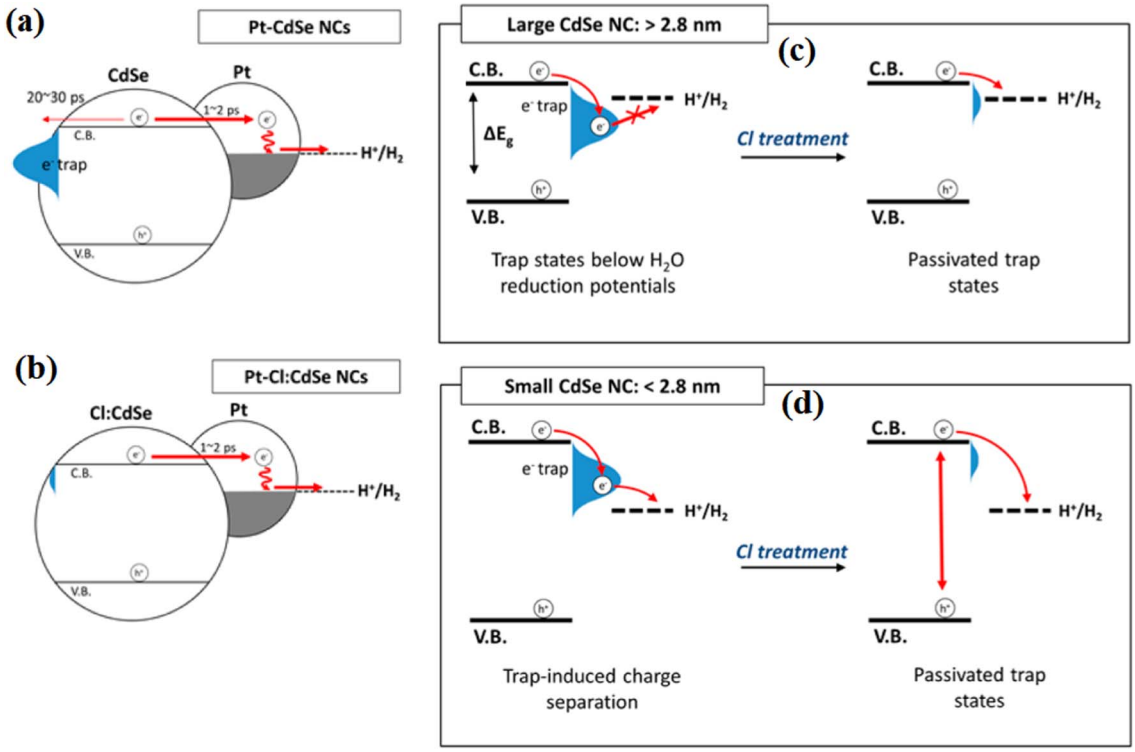

Fig. 23 Electron dynamics in (a) Pt-CdSe and (b) Pt–Cl:CdSe NCs. (c) and (d) Illustration of the effect of Cl on surface traps at different NC size ranges during photocatalytic hydrogen generation. Reproduced with permission from ref. 103. Copyright 2016, the American Chemical Society.

between semiconductors often causes serious distortion and mismatch at the interface. Lattice distortion at the interface creates a high density of defect states at the interface, where the formed defects act as trapping sites for charge carriers and result in decreased photocatalytic ability.[105,106] In the long term, the performance of photocatalytic systems was found to be much lower than expected, and one of the main factors for this is the harmful charge recombination caused by doping, vacancy, plastic deformation, and interface lattice mismatch. To date, these shortcomings have seriously limited the design and fabrication of high-performance heterostructure photocatalysts. Thus, by using an interfacial passivation strategy, the above-mentioned long-term issue in heterostructures is expected to be resolved, significantly improving the separation efficiency of charge carriers.

In general, to passivate interfacial defects, some materials with an amorphous structure or good interface compatibility are introduced, where the core aim is to release the interfacial stress between semiconductors. At the same time, the interfacial passivation layers act as a tunneling barrier to inhibit the

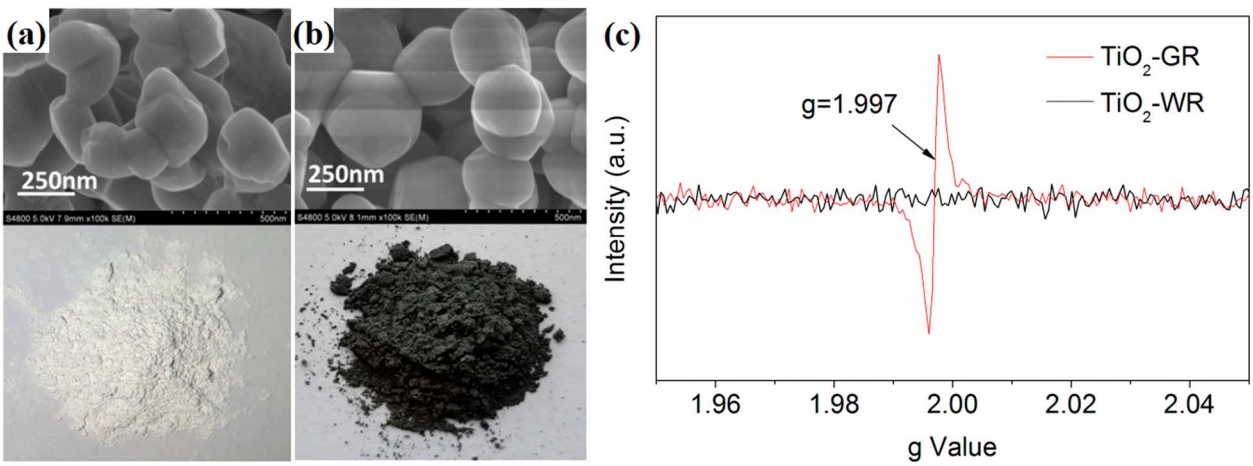

Fig. 24 (a and b) Morphology of TiO_2-gray rutile (TiO_2-GR) and TiO_2-white rutile (TiO_2-WR). (c) EPR spectra of TiO_2-GR and TiO_2-WR. Reproduced with permission from ref. 59. Copyright 2020, MDPI.

interfacial charge carrier recombination and passivate the surface states, which can reduce the non-radiative carrier recombination. In addition, some passivation materials are equipped with a special charge effect, which usually results in improved charge transport in the host semiconductors.

5.2.1 Releasing interface stress. The most adopted method is to insert a material with good interfacial compatibility as a passivation layer between materials. Inspired by the role of GO as a buffer layer to improve the charge transfer in the structural design of organic photovoltaic devices, Dai *et al.*[107] fabricated a g-C_3N_4/BiOI/GO ternary nanocomposite using GO as a buffer material. The introduced GO provides lower interfacial band barriers than that of the directly contacted g-C_3N_4/BiOI interface, thus significantly enhancing the photocatalytic performance of the composite. Similarly, hybrid structures composed of rGO and CdSe@ZnO nanostructures were synthesized *via* a hydrothermal method for photoelectrochemical water splitting.[108] The functions of rGO in these structures were analyzed by decorating rGO on ZnO and CdSe surfaces. When rGO was inserted in the interface between ZnO and CdSe, the interface resistance decreased, which contributed to enhanced charge transmission. Thus, a high photocurrent density of 6.5 mA cm^{-2} was obtained for the above-mentioned photoanode, which was 1.2 times that of the CdSe@ZnO structure. In the case of CdSe@ZnO NAs loaded with rGO at the CdSe surface, the corrosion of the photoanode was alleviated due to the surface passivation function of rGO, which effectively prolonged the carrier lifetime and improved the device stability. Based on this, under the condition of both ZnO and CdSe surfaces being covered by an rGO layer, the charge transmission and anti-photo-corrosion ability were simultaneously enhanced.

To gain an in-depth understanding of the role of the interfacial passivation layer in hybrid systems, our group[57] fabricated a CdS@Al_2O_3@ZnO photocatalyst by introducing atomic-level ultrathin Al_2O_3 between CdS and ZnO through the ALD method, where an intimately contacted interface could be formed under the passivation effect of the Al_2O_3 layer (Fig. 25a–c). The as-fabricated sample displayed PHE ability depending on the thickness of Al_2O_3 (Fig. 25e). DFT calculation revealed that the introduced Al_2O_3 efficiently decreased the contact potential between CdS and ZnO, and thus contributed to the rapid transfer of charge carriers (Fig. 25d). In addition, the photogenerated holes were consumed efficiently by the fixed negative charges of the Al_2O_3 ultrathin layer, and thus converted the original Z-scheme mechanism of photogenerated charge carriers in the CdS@ZnO catalyst into a modified type II mechanism in the CdS@Al_2O_3@ZnO catalyst, which guaranteed sufficient contact between electrons and H_2O (Fig. 25f and g).

Huang *et al.*[109] introduced an S_x–In–P_{1-x} passivation monolayer in the interface between InP and ZnS, where the S_x–In–P_{1-x} monolayer passivated the defects in the original InP, which inhibited the undesirable photogenerated charge recombination at the trap sites and resulted in positive effects for photocatalytic H_2 evolution. At the same time, the passivation monolayer decreased the lattice mismatch between the InP core and ZnS shell, further eliminating the interfacial defect sites in the hybrids. Furthermore, the formed alloyed interface also played a vital role in spreading out the radial probability density of electrons and holes, while the delocalization of excitons to the buffer layer was beneficial for their tunneling out of InP.

Another negative effect caused by interfacial stress is the agglomeration of catalysts, which reduces the effective contact between semiconductors and results in a limited interface electric field. Focusing on this issue, by encapsulating SnO_2 QDs with a thin carbon layer, Yan *et al.*[62] anchored SnO_2 quantum dots (QDs) on the surface of g-C_3N_4 nanosheets and efficiently avoided the aggregation of SnO_2 QDs. As shown in Fig. 26, theoretical calculations revealed that carbon encapsulation can stabilize the SnO_2 QDs and strengthen the interaction between SnO_2 and g-C_3N_4 nanosheets, and thus a strong internal electric field can be formed at the intimate interface between SnO_2 and g-C_3N_4, is which beneficial for the separation and one-directional migration of photogenerated charge carriers. To construct a stable contact between FTO glass and photocatalyst, Chen *et al.*[58] deposited an interfacial anatase TiO_2 seed layer prior to the growth of rutile TiO_2 nanorods, which led to 34% enhanced photocatalytic H_2 evolution performance of the sample. The interfacial charge-carrier dynamics studies revealed that the anatase TiO_2 seed layer was beneficial for better energy band alignment and boosted charge collection at the interface of TiO_2 NR/FTO.

5.2.2 Decreasing interface defects. Besides, interface defects are one of the most detrimental factors for inefficient photocatalytic hydrogen evolution by nanocomposites, and thus the efficient passivation of interface defects can enhance their photocatalytic performance. In this case, a simple and creative strategy is to passivate the interface defects through the introduction of interfacial chemical bonding.[30–32,60–62] For example, Zheng *et al.*[60] constructed P-doped C_3N_4 (P-C_3N_4) *via* the thermal polymerization of urea with phytic acid as a P source. The doped P atoms could act as anchoring sites for photo-deposited Ni nanoparticles (NPs) on P-C_3N_4, and Ni–P–N bonds were spontaneously formed between Ni NPs and P-C_3N_4 with doped P as the bridging ligand (Fig. 27a and c). Consequently, the introduction of P resulted in a 6 times higher H_2 evolution rate than the sample without P doping (Fig. 27b). At the same time, Gai *et al.*[32] introduced Co atoms in C_3N_4/CdS/Ni and constructed an NiCo dual-metal cocatalyst system, and it was found that a Co–S bond can be formed between CdS and the NiCo cocatalyst (Fig. 27d), which can accelerate the vectorial charge transfer and improve the stability of the photocatalysts. Furthermore, theoretical calculation demonstrated that the introduction of Co can efficiently decrease the Gibbs free energy of the Ni cocatalyst (Fig. 27e), indicating the enhanced proton adsorption and product desorption in the CoNi alloyed NPs. Thus, the CoNi cocatalyst-decorated sample displayed much higher H_2 evolution ability than that of the Ni-decorated C_3N_4/CdS photocatalyst (Fig. 27f). Shen *et al.*[80] investigated the interface structure between NiP and black phosphorus and found that the formation of an interface Ni–P bond acted as an atomic-level electron transfer channel to reduce the potential energy barrier for interface charge transfer, thus resulting in enhanced photocatalytic activity.

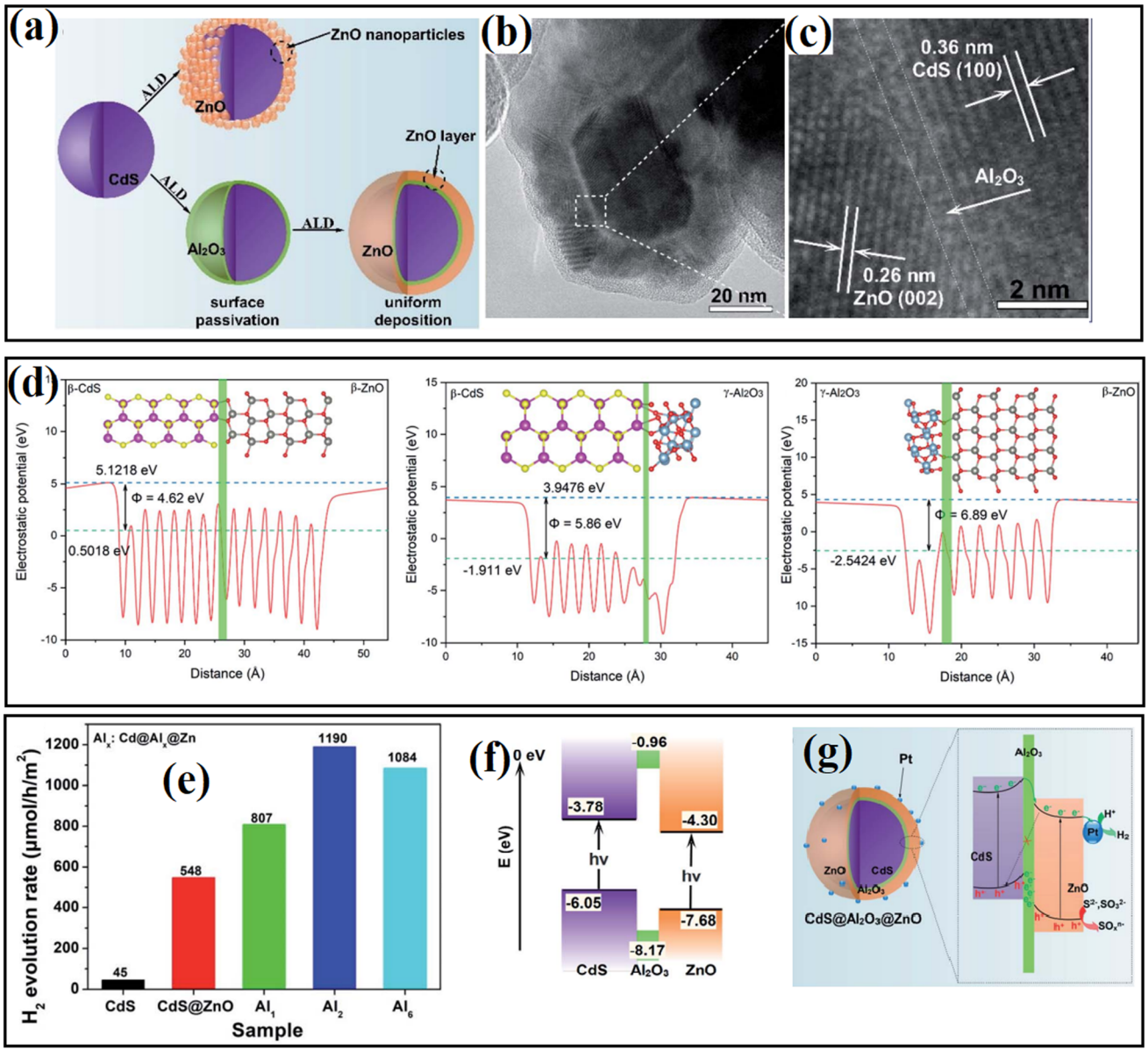

Fig. 25 (a) Schematic view of the preparation of Cd@Al@ Zn. (b and c) TEM and HR-TEM images of Cd@Al@ Zn. (d) Calculated slab module of energy change along the *c* direction of the slab cell for CdS–ZnO, CdS–Al_2O_3 and Al_2O_3–ZnO interfaces. (e) Comparison of photocatalytic H_2 generation rates over the as-fabricated samples with different deposition thickness of Al_2O_3. (f) Calculated energy band position of CdS, Al_2O_3 and ZnO. (g) Possible energy transfer mechanism in Cd@Al@Zn. Reproduced with permission from Ref [57]. Copyright 2020, the Royal Society of Chemistry.

Besides inserting a thin passivation layer into semiconductors, some impurity atoms can also lead to improved interfacial properties, thus benefiting the photocatalytic reaction. Zhang *et al.*[61] systematically studied the interfacial properties of an MoS_2/GaN 2D/3D heterostructure by inserting a nitridation interfacial layer at the MoS_2/GaN interface through remote N_2 plasma treatment. It was found that the introduction of N atoms efficiently increased the average bond length between the N adatoms and the surface Ga atoms from 2.03 Å to 2.27 Å due to the strong interfacial interaction, where both the CB and VB of MoS_2 move upward relative to the GaN side, leading to an increase in the band offsets in this type-II alignment (Fig. 28a and b). At the same time, the introduced indirect band gap caused by N atoms prevented the recombination of photoexcited electrons and holes (Fig. 28c and d). Although the N atoms resulted in a decrease in the band gap of the system, where the CB of the samples was located in the proper position for the splitting of water (Fig. 28e), which indicates an ideal potential in the PHE reaction. More importantly, a notable enhancement in the energy absorption in the range of 2–3 eV was observed for the heterostructure that underwent interface nitridation, implying its potential application as an excellent light harvester (Fig. 28f). This work has demonstrated that treating the interface of heterostructures by using proper atoms is a promising way in efficiently increasing the stability and activity of photocatalysts.

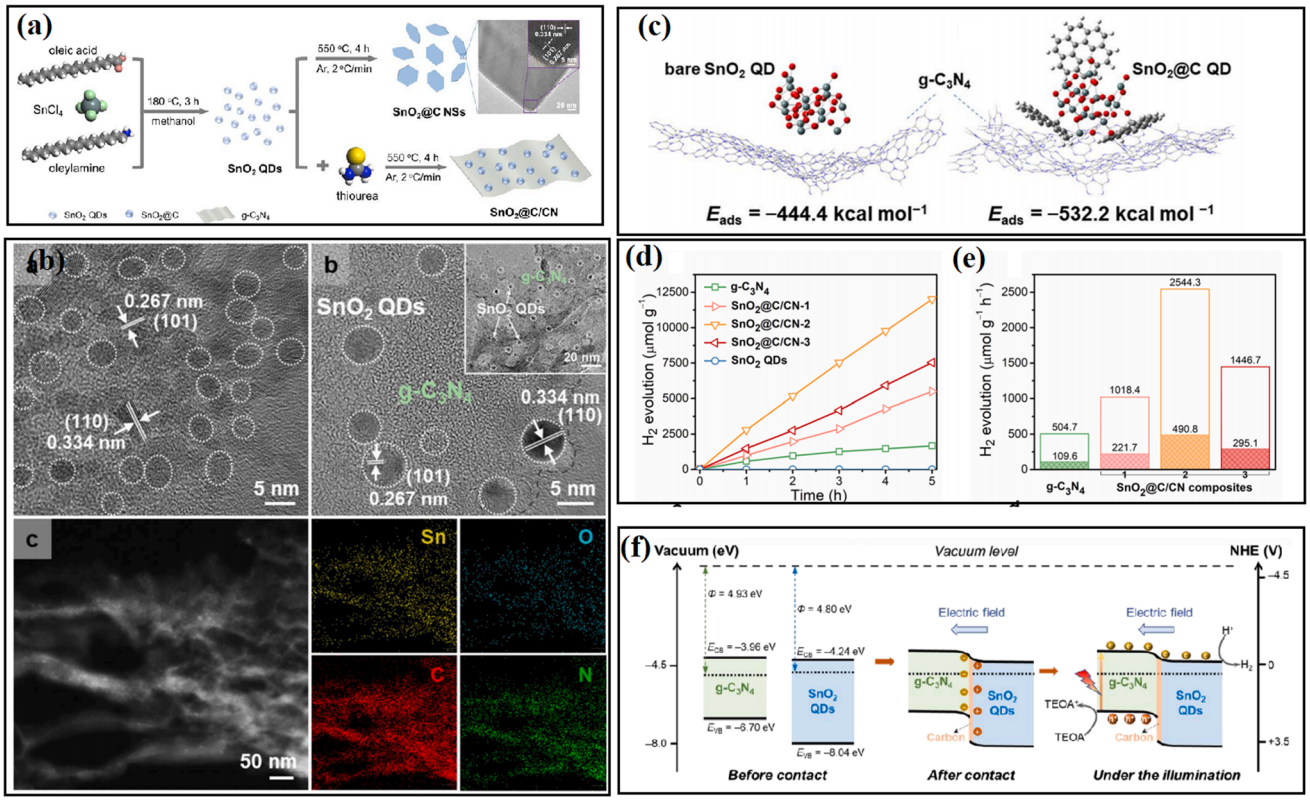

Fig. 26 (a) Overview of the synthetic procedure for SnO_2@C/CN. TEM image is SnO_2@C NSs. (b) TEM image, HRTEM and EDX elemental mapping images of SnO_2@C/CN-2. (c) Side-views of the adsorption configurations of (left) bare SnO_2 and (right) SnO_2@C QDs on g-C_3N_4 surface. (d) Photocatalytic H_2 evolution in 5 h and (e) photocatalytic H_2 evolution rate over the samples. (f) Proposed band alignment and mechanism of photocatalytic H_2 evolution involved in the SnO_2@C/CN. Reproduced with permission from ref. 62. Copyright 2021, Elsevier.

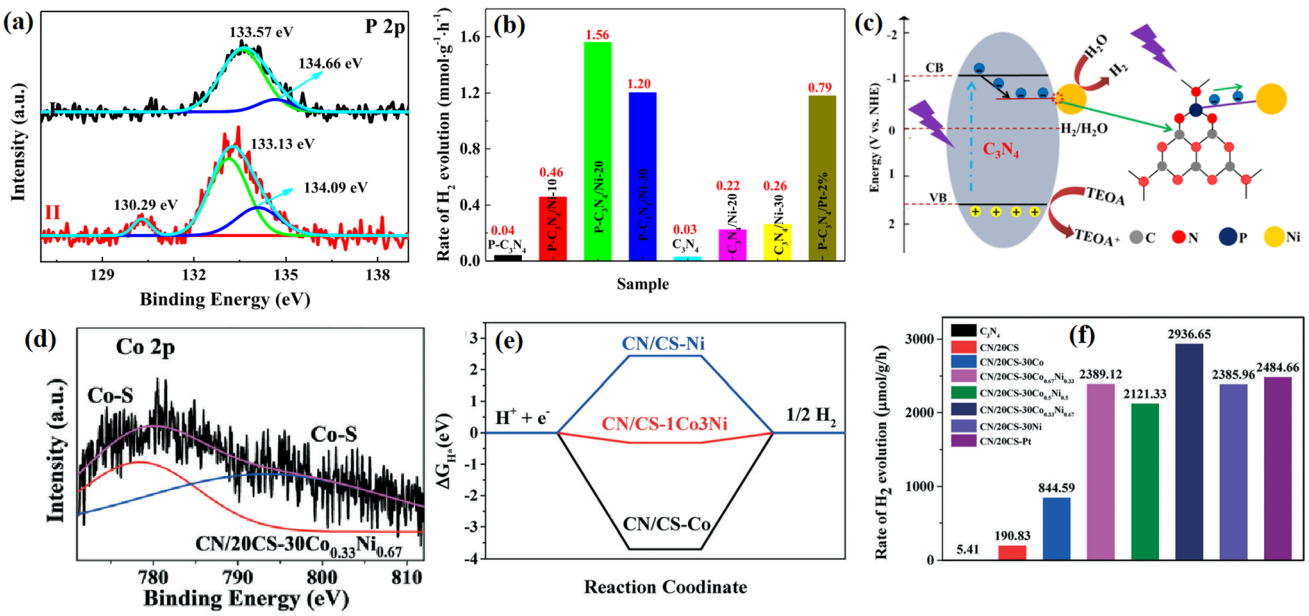

Fig. 27 (a) XPS of P 2p in P-C_3N_4 and P-C_3N_4/Ni-20. (b) Photocatalytic H_2 evolution rates of photocatalysts. (c) Schematic of the photocatalytic H_2 production mechanism of P-C_3N_4/Ni-20. (d) XPS of Co 2p in CN/20CS-30 $Co_{0.33}Ni_{0.67}$. (e) Gibbs free energy for proton adsorption on CN/CS-Co, CN/CS-1Co3Ni and CN/CS-Ni, and (f) H_2 evolution rates of the samples. Reproduced with permission from ref. 60. Copyright 2022, the American Chemical Society.

Choi and co-workers[33] deposited a TiO_2 layer between InAs nanowires (NWs) and p-Si by the ALD strategy, and it was found that TiO_2 effectively passivated the vulnerable InAs NWs and the Pt co-catalyst prevented the accumulation of photogenerated electrons on the surface of TiO_2. In this system, the self-reduction of the TiO_2 passivation layer was suppressed by the outer Pt, and thus the obtained catalyst system displayed good stability over 20 h (Fig. 29).

In Devarapalli's[34] report, a thin carbon layer was introduced in the interface between Si nanowires (SiNWs) and TiO_2 to reduce the number of defect sites and protect against oxidation in the air or water. Specifically, the surface of hydrogen-terminated SiNWs was firstly chemically functionalized using a photochemical alkylation method, and subsequently the functionalized surface was converted into an ultra-thin passivation layer of carbon by annealing at high temperature. The introduced carbon layer efficiently decreased the charge recombination rates and enhanced the interfacial charge transfer between the silicon and TiO_2. As shown in Fig. 30a and b, based the observation of flat band potential values, it was confirmed that the carbon passivation layer did not change the properties of silicon except perhaps passivating the defects on the surface of the silicon nanowires. It was found that the donor densities (Nd) for C@SiNWs were an order of magnitude higher than that for SiNWs, demonstrating that the introduction of a carbon passivation layer resulted in higher carrier generation and lower recombination losses. In addition, the corresponding photoelectric chemical performance tests showed that the carbon-modified sample displayed much higher photoelectric transfer ability (Fig. 30c and d). The formation of a carbon layer efficiently suppressed the recombination of electrons and holes, reduced the number of defect sites, and improved the interfacial charge transfer between SiNWs and TiO_2. As a result, the optimized sample displayed 2.78 times higher water splitting efficiency than that on the non-passivated sample.

In summary, the formation of a well-contacted interface in an interfacial passivation system is mainly due to the special structures of the passivation layer or the existence of strong chemical bonding between the passivation layer and substrates. In general, there are two types of materials that can be utilized for interfacial

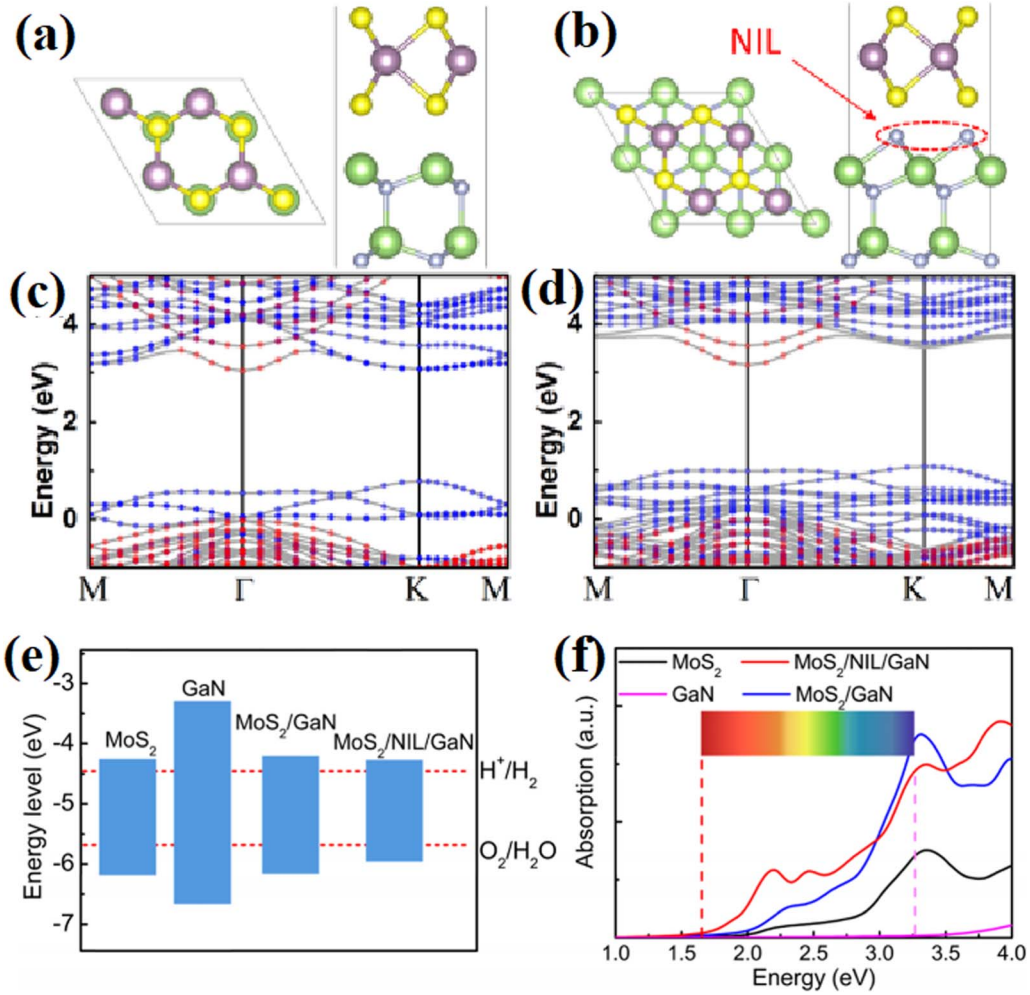

Fig. 28 (a and b) Atomic structures of MoS_2/GaN heterostructure without and with nitridation interfacial layer. Both the top and side views are demonstrated. (c and d) Corresponding energy band structures. The red (blue) dotted region presents the isolated GaN (MoS_2) band structure. (e) Band edge positions of the samples with reference to the vacuum level. (f) Calculated absorption spectra of the samples. Reproduced with permission from ref. 61. Copyright 2018, the American Chemical Society.

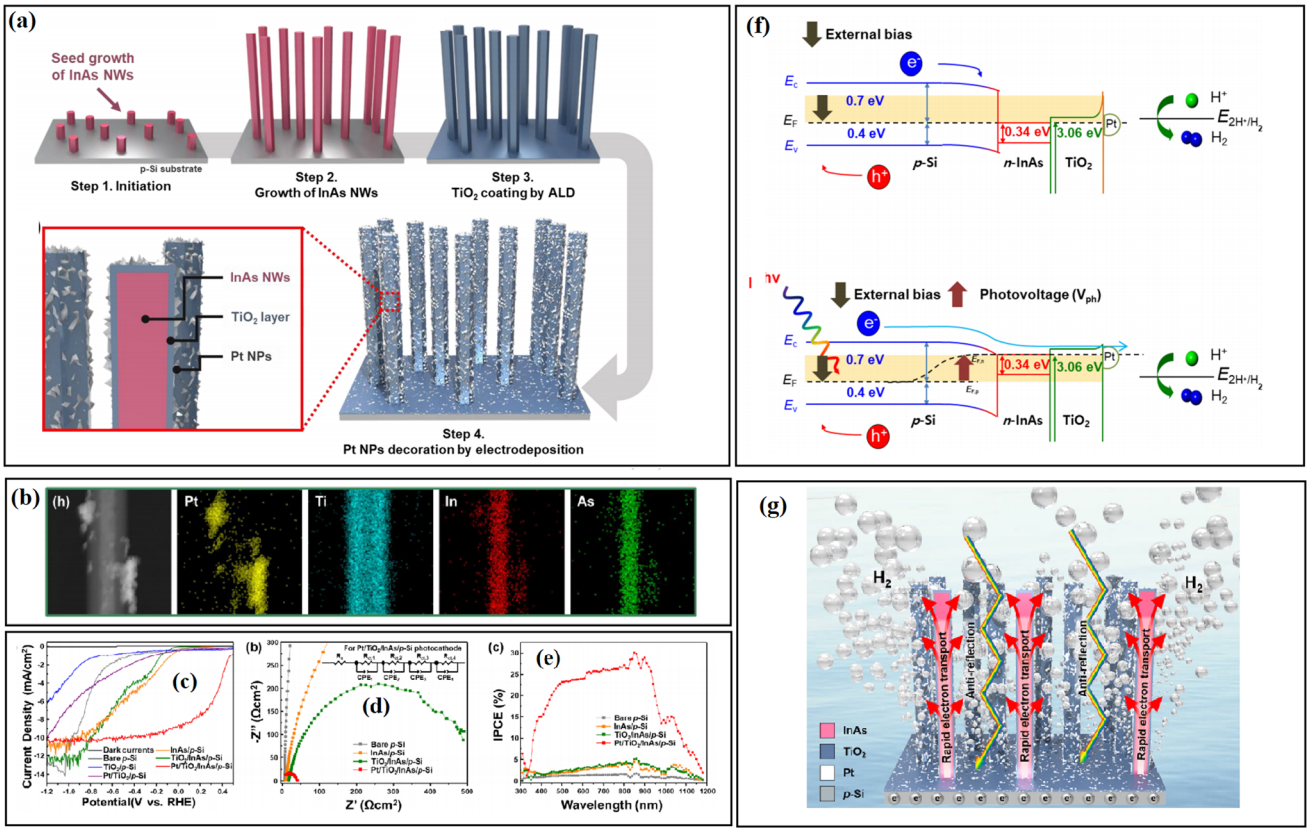

Fig. 29 (a) Schematic diagrams of experimental procedures, photographic image, and optical reflectance. (b) HAADF-EDS mapping images of the TiO_2/InAs NWs/p-Si photocathode. (For interpretation of the references to colour in this figure legend, the reader is referred to the web version of this article.) (c) *J*–*V* curves of the heterostructure photocathodes, (d) EIS spectra and (e) incident-photon-to-current conversion efficiency measurements of the samples. (f) Energy band diagram of the Pt/TiO_2/InAs NWs/p-Si photocathodes at 0.48 V *vs.* RHE under dark (top) and illumination (bottom). (g) Illustration of the H_2 evolution mechanism in TiO_2/InAs NWs/p-Si. Reproduced with permission from ref. 33. Copyright 2020, Elsevier.

passivation. (1) Materials with an amorphous crystal structure, in which the loose and irregular arrangement of atoms endows the material with good surface compatibility. When combined with semiconductors, the adjustable arrangement of atoms guarantees the formation of an intimately contacted semiconductor-passivation layer interface at the atomic level. Subsequently, when a secondary semiconductor is introduced, a well-contacted passivation layer-semiconductor interface will be formed at the other side of the passivation layer. Thus, the passivation layer serves as an interfacial bridge to provide a soft buffer region and efficiently release the interfacial stress between directly contacted semiconductors. (2) Materials capable of forming strong chemical bonds with semiconductors. During some special treatment procedures, such as high temperature, the formation of strong chemical bonding efficiently declines the density of defects and serves as a bonding bridge between two semiconductors, thus contributing to the formation of a well-contacted interface.

5.3 Key factors and strategies controlling the influence of the effect of passivation engineering

Based on numerous reports, it can be found that the passivation layer often functions as a double-edged sword, and thus it cannot be concluded that the presence of a passivation layer with result in a higher photocatalytic performance. Many materials used in passivation engineering are inert or only have very low activity in PHE, and the introduction of a surplus passivation layer will lead to an increase in the proportion of non-active components, which not only leads to a decline in photocatalytic activity at the same mass, but also increases the catalytic cost.[81,90,92] Moreover, most of the passivation materials are not universal in all systems, and the materials that show an enhanced effect on some substrates may lead to a decrease in catalytic performance on others, which depends on the basic electrochemical properties of passivation materials and interaction between the passivation layer and the substrates. It can be seen that the thickness and type of passivation materials are the two dominant factors that should be considered. In the following content, we will give a detailed introduction on the influence of these two key factors on the passivation layer and the regulation strategies.

5.3.1 Thickness of the passivation layer. In particular, the thickness of the passivation layer has a great influence on the PHE of photocatalysts. In the case of surface passivation, the over introduction of a passivation layer may shield the exposed active reaction sites and result in decreased light harvest

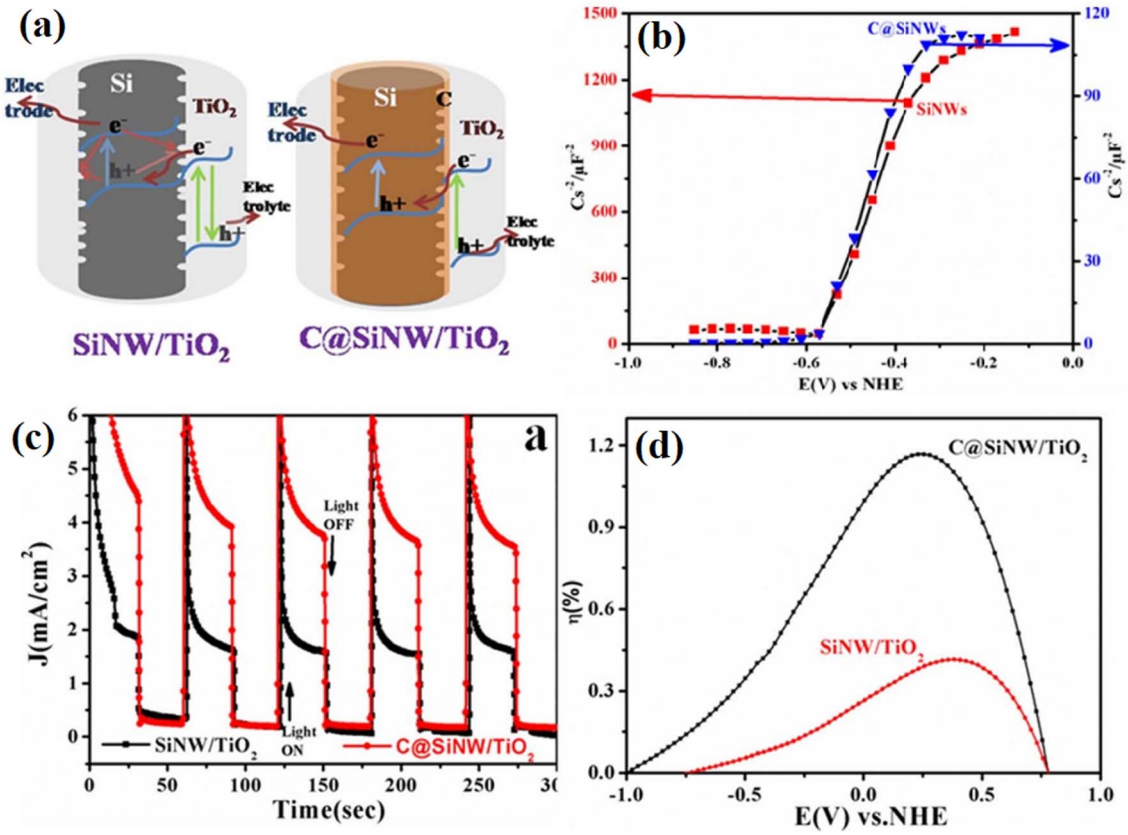

Fig. 30 (a) Proposed electron transfer mechanism in SiNW/TiO_2 and C@SiNW/TiO_2 core–shell nanowire arrays. (b) Mott–Schottky plots of SiNWs and C@SiNWs measured at 5 kHz. (c) Chronoamperometric graphs under light off and on conditions of C@SiNWs/TiO_2 and SiNWs/TiO_2 nanowires. (d) Photoconversion efficiencies of the samples as a function of measured potentials. Reproduced with permission from ref. 34. Copyright 2014, Springer.

capacity, resulting in a decline in PHE ability. Similarly, for interfacial passivation, a too thick passivation layer may in reverse act as a charge barrier to hinder the rapid migration of charge carriers between semiconductors. Despite the formation of a well-contacted interface, the tunneling effect in the modified system with ultra-thin passivation layer is also important in accelerating the charge transfer when the passivation layer is thinner than 2 nm.[54,110] However, the interfacial passivation layer should be as thin as possible because an ultrathin layer may increase the possibility of generating weak points, such as cracks and pinholes, which may seriously destroy the effect of the passivation layer. Therefore, precisely controlling the thickness of the passivation layer is also an important task in passivation engineering.

The ALD method is regarded as one of the most efficient methods for precisely controlling the thickness of the passivation layer, by which the covering thickness can be changed at the atomic level due to the self-limited deposition property through the deposition cycle times. ALD can be used in the formation of both surface passivation and interfacial passivation layers and their thickness. For example, Liu and coworkers[111] deposited a TiO_2 shell on ZnO nano-arrays through the ALD method, and a nearly 90% declined deep-level PL emission could be achieved when the thickness of TiO_2 decreased to about 1 nm, indicating the efficient removal of the deep hole traps through the surface passivation. In another example,[55] an ALD method was utilized to deposit a TiO_2 passivation layer between CdS and ZnO, and a 20 nm passivation TiO_2 layer was found to be the most efficient in obtaining the highest H_2 evolution ability. In our previous work,[57] by changing the ALD deposition cycle from 1, 2, 4, to 10 times, it was found that an ultrathin passivation layer with 2 cycles of Al_2O_3 deposition resulted in the most improved H_2 evolution rate.

Some other deposition methods, such as chemical vapor deposition (CVD) and ion sputtering method, are also utilized for the introduction of a passivation layer, and the deposition cycle and deposition times are two crucial parameters in controlling the thickness of the passivation layer. In 2013, Seger *et al.*[112] modified Si-based photoelectrodes using TiO_2 as a conductive passivation layer. The thickness of the TiO_2 layer could be controlled by the sputtering time, and a sputtered 100 nm passivation layer was proven to be the most effective in protecting the surface of the Si substrate from corrosion.

In addition to deposition strategies, high-temperature treatment is also a common method in passivation engineering. For example, in the reported CdS/CdZnS/ZnO system,[63] the CdZnS passivation layer was formed at the interface between CdS and ZnO under high-temperature condition, with

the gradual consumption of CdS and ZnO. The heating temperature had an obvious effect on the formation and content of the passivation layer. When the heating temperature was too low, the formation of CdZnS was too small to totally passivate the interface defects between CdS and ZnO, but a too high temperature led to a dramatically declined PHE performance due to the over consumption of photocatalytic active components (CdS and ZnO). Similarly, in the work by Yan and coworkers,[62] the relative content of carbon passivation layer in an SnO_2 QD-deposited g-C_3N_4 system could be controlled by tuning the additive amount of precursors. However, in these heating strategies, it is difficult to precisely control to the thickness of the passivation layer. By controlling some key parameters, such as additive amount of precursors, the reaction time, and reaction temperature, the relative content of passivation layer can be controlled in a qualitative aspect.

5.3.2 The categories of passivation material. Besides the thickness, the materials utilized in the passivation layer is another crucial factor affecting the efficiency of passivation engineering. Although the aim of passivation is to reduce the adverse factors that affect the transfer and utilization of charge carriers, as well as the stability of catalysts, and unavoidable fact is that many passivation materials, including the above-mentioned TiO_2, ZnS, ZnO, and GO,[55,65–69,78,82,96,97] have special electrochemical properties and inherent catalytic properties. Consequently, the passivation layer should not been seen as a totally chemical inert component, and its basic properties, such as light absorption property, charge transfer ability, and inherent electrochemical properties should also be considered in the design and selection of passivation layer-modified systems. For example, Al_2O_3 was reported to have numerous fixed negative charges, and thus have the ability to harvest photogenerated holes.[35,57,70] Thus, by depositing Al_2O_3 at the interface of CdS and ZnO, we successfully constructed a new type II heterostructure by transferring electrons from the CdS core towards the ZnO shell through an Al_2O_3 bridge.[57]

To date, the study on the effect of materials on passivation engineering has mainly focused on the ion-induced surface passivation system. Liu *et al.*[104] studied the effect of edge passivation of halogen ions on the PHE of Sb nanoribbons. In all the samples, the introduction of halogen ions is useful for improving the stability and benefiting the light absorption. At the same time, the halogen ions display different tuning effects in changing the band edges and band gaps of Sb, and only the F-decorated sample matched the REDOX potentials of PHE. Agrawal *et al.*[113] studied the influence of halogen (F, Cl, Br, and I) passivation on the electronic structure of zigzag graphene nanoribbons (ZGNRs). They found that the stability of the halogen-passivated ZGNRs followed the order of F > Cl > Br > I, while the I- and Br-passivated samples had relatively higher current–voltage characteristics than the F- and Cl-passivated samples. Neuderth and coworkers[90] studied the influence of ultra-thin TiO_2, CeO_2 and Al_2O_3 passivation layers on the photocatalytic properties of InGaN. They found that the 5 nm TiO_2-passivated sample displayed an increase in anodic photocurrent, whereas a decreased photocurrent was observed for the CeO_2- and Al_2O_3-coated sample due to the enhanced defect recombination in the passivation layer or increased band discontinuities. Furthermore, the photocatalytic ability of the InGaN NW decreased due to the TiO_2 layer and was even completely suppressed when the thickness of the TiO_2 layer reached to 7 nm or more. This work fully demonstrated the important influence of the type and thickness of the passivation layer materials on the properties of the substrate materials.

In addition, it is foreseeable that the impact of passivation materials on the passivation effect is also reflected in the type and strength of the interaction between the passivation layer and the substrate. However, to the best of our knowledge, there is still lack of systematic study on the relationship between the types of materials in the passivation layer and their passivation effect. With the development of passivation engineering in the photocatalytic field, we believe that related studies will be reported in the near future.

6. Conclusions and outlook

Photocatalytic hydrogen evolution provides an eco-friendly and sustainable pathway to address the issues related to the energy and environment, but the low activity and poor stability of photocatalysts have long restricted the promotion and application of PHE technology. In this case, passivation is an efficient and promising strategy in protecting the vulnerable surface from the environment and buffering the recombination of charges from the defective interface. Focusing on the various problems in different catalysts, different passivation methods can be adopted to eliminate the defects, protect the susceptible surface, and construct an intimately contacted interface, thus suppressing the harmful charge recombination and photocorrosion, and ultimately improving the photocatalytic activity and durability of catalysts. This review presented a comprehensive overview of passivation engineering ranging from its basic principles, roles, fabrication methods, and characterization methods to its application in interfacial passivation and surface passivation. However, despite the significant advances to date, the study of passivation technology is still limited. Thus, to make full use of passivation engineering to improve the performance of photocatalysts, the following factors are worth exploring in future studies.

(1) There is still much debate regarding the mechanism of passivation-modified catalysts, especially in core–shell structure photocatalysts. Some researchers ascribe the improvement in hydrogen evolution ability to the formation of a heterostructure but ignore the passivation effect caused by the covering layer, while other researchers tend to emphasize the role of the shell in eliminating defects or suppressing charge recombination as a passivation layer, but the photocatalytic ability of the passivation layer itself is neglected. Therefore, to comprehensively reveal the mechanism of photocatalysis, the existence of a passivation layer and its effects need to be accurately identified and fully verified.

(2) The introduction of passivation engineering is useful in improving the photocatalytic performance, but the control and optimization of the passivation degree still require significant efforts. As mentioned, some defects can be eliminated through

the appropriate passivation treatment, but it was also reported that the existence of defects contributes to the separation of charge carriers. In this case, it is a challenge to accurately detect the type and function of defects and eliminate unfavorable defects and retain favorable defects by appropriate passivation means.

(3) Characterization methods still lag behind the development of synthetic methods, which presents an obstacle in investigating the effects and mechanisms of passivation engineering. For instance, the formation, spatial distribution and concentration of surface and interface defects have a deadly effect on the transfer and separation of charge carriers, but these features still cannot be accurately characterized by prior characterization means. In addition, to deepen the understanding on the contribution of passivation engineering to photocatalytic performance, some *in situ* studies at high spatial and temporal resolutions are also urgently needed.

(4) Although ALD is widely adopted in the deposition of a passivation layer, the large-scale use of this technology is still unrealistic in a short time because of the high-cost precursors and trivial technological operation. Thus, new methods need to be developed to construct passivation systems with high efficiency, good controllability and low cost.

Conflicts of interest

The authors declare no conflict of interest.

Acknowledgements

This work was sponsored by the National Natural Science Foundation of China (21972110), the Postdoctoral Science Foundation of China (2021M692535), the Natural Science Foundation of Shaanxi Province (2022JQ-095), the Basic Research Project Foundation of Xi'an Jiaotong University (xzy012024012), and the Youth Foundation of State Key Laboratory of Electrical Insulation and Power Equipment (EIPE2131).

References

1 M. Qi, M. Conte, M. Anpo, Z. Tang and Y. Xu, *Chem. Rev.*, 2021, **121**, 13051–13085.
2 Y. Li, S. Yu, J. Xiang, F. Zhang, A. Jiang, Y. Duan, C. Tang, Y. Cao, H. Guo and Y. Zhou, *ACS Catal.*, 2023, **13**, 8281–8292.
3 M. Rahman, T. Edvinsson and J. Gascon, *Nat. Rev. Chem.*, 2022, **6**, 243–258.
4 Q. Wang and K. Domen, *Chem. Rev.*, 2020, **120**, 919–985.
5 D. Maarisetty and S. Baral, *J. Mater. Chem. A*, 2020, **8**, 18560.
6 Z. Kang, H. Si, S. Zhang, J. Wu, Y. Sun, Q. Liao, Z. Zhang and Y. Zhang, *Adv. Funct. Mater.*, 2019, **29**, 1808032.
7 X. Wang, C. Zhou, W. Wang, B. Du, J. Cai, G. Feng and R. Zhang, *J. Alloys Compd.*, 2018, **747**, 826–833.
8 H. Ren, K. Ye, H. Chen, F. Wang, Y. Hu, Q. Shi, H. Yu, R. Lv and M. Chen, *Colloids Surf., A*, 2022, **652**, 129844.
9 G. Cheng, S. Li, C. Wang and J. Xiong, *Adv. Energy Sustainability Res.*, 2023, **4**(7), 2300002.
10 D. Ma, J. Shi, L. Sun, Y. Sun, S. Mao, Z. Pu, C. He, Y. Zhang, D. He, H. Wang and Y. Cheng, *Chem. Eng. J.*, 2022, **431**, 133446.
11 R. Singh and S. Dutta, *Fuel*, 2018, **220**, 607–620.
12 W. Ma, D. Zheng, B. Xiao, Y. Xian, Q. Zhang, S. Wang, J. Liu, P. Wang and X. Hu, *J. Environ. Chem. Eng.*, 2022, **10**(3), 107822.
13 L. Cheng, Q. Xiang, Y. Liao and H. Zhang, *Energy Environ. Sci.*, 2018, **11**, 1362–1391.
14 Y. Zou, J. Shi, D. Ma, Z. Fan, C. He, L. Cheng, D. Sun, J. Li, Z. Wang and C. Niu, *Catal. Sci. Technol.*, 2018, **8**, 3883–3893.
15 Y. Zhi, Y. Yi, C. Deng, Q. Zhang, S. Yang and F. Peng, *ChemSusChem*, 2022, **15**, e202200860.
16 G. Lee and J. Wu, *Powder Technol.*, 2017, **318**, 8–22.
17 C. Chang, K. Chu, M. Hsu and C. Chen, *Int. J. Hydrogen Energy*, 2015, **40**, 14498–14506.
18 J. Shi, Y. Zou, D. Ma, Z. Fan, L. Cheng, D. Sun, Z. Wang, C. Niu and L. Wang, *Nanoscale*, 2018, **10**, 9292–9303.
19 J. Shi, Y. Zou, L. Cheng, D. Ma, D. Sun, S. Mao, L. Sun, C. He and Z. Wang, *Chem. Eng. J.*, 2019, **378**, 122161.
20 S. Mao, J. Shi, G. Sun, Y. Zhang, D. Ma, K. Song, Y. Lv, J. Zhou, H. Wang and Y. Cheng, *ACS Appl. Mater. Interfaces*, 2022, **14**, 48770–48779.
21 Y. Lv, D. Ma, C. Yang, K. Song, L. Shi, Y. Cheng, C. Niu and J. Shi, *Sep. Purif. Technol.*, 2023, **316**, 123813.
22 P. Madhusudan, Y. Wang, B. Chandrashekar, W. Wang, J. Wang, J. Miao, R. Shi, Y. Liang, G. Mi and C. Cheng, *Appl. Catal., B*, 2019, **253**, 379–390.
23 J. Lin, Y. Yan, T. Xu, J. Cao, X. Zheng, J. Feng and J. Qi, *J. Colloid Interface Sci.*, 2020, **564**, 37–42.
24 C. Liu, T. Gong, J. Zhang, X. Zheng, J. Mao, H. Liu, Y. Lia and Q. Hao, *Appl. Catal.; B*, 2020, **262**, 118245.
25 Y. Lv, D. Ma, K. Song, S. Mao, Z. Liu, D. He, X. Zhao, T. Yao and J. Shi, *J. Mater. Chem. A*, 2023, **11**, 800–808.
26 S. Mao, J. Shi, G. Sun, Y. Zhang, X. Ji, Y. Lv, B. Wang, Y. Xu and Y. Cheng, *Chem. Eng. J.*, 2021, **404**, 126533.
27 D. Ma, J. Shi, Z. Pu, S. Mao, X. Xu, D. He, R. Guo and F. Chen, *Sol. RRL*, 2022, **6**, 2200714.
28 Y. Yang, Y. Liu, B. Mao, B. Luo, K. Zhang, W. Wei, Z. Kang, W. Shi and S. Yuan, *Catal. Lett.*, 2019, **149**, 1800–1812.
29 S. Yang, D. Prendergast and J. Neaton, *Nano Lett.*, 2012, **12**, 383–388.
30 C. Li, M. Gao, X. Sun, H. Tang, H. Dong and F. Zhang, *Appl. Catal., B*, 2020, **266**, 118586.
31 R. Zhong, Z. Zhang, H. Yi, L. Zeng, C. Tang, L. Huang and M. Gu, *Appl. Catal., B*, 2018, **237**, 1130–1138.
32 Q. Gai, S. Ren, X. Zheng, W. Liu and Q. Dong, *Catal. Sci. Technol.*, 2021, **11**, 5579–5589.
33 S. Choi, J. Hwang, T. Lee, H. Kim, S. Hong, C. Kim, M. Choi, H. Park, S. Bhat, J. Suh, J. Lee, K. Choi, S. Hong, J. Shin and H. Jang, *Chem. Eng. J.*, 2020, **392**, 123688.
34 R. Devarapalli, J. Debguptal, V. Pillai and M. Shelke, *Sci. Rep.*, 2014, **4**, 4897.
35 H. Cheng, F. Wang, J. Chu, R. Santhanam, J. Rick and S. Lo, *J. Phys. Chem. C*, 2012, **116**, 7629–7637.

36 N. Elumalai, C. Vijila, R. Jose, A. Uddin and S. Ramakrishna, *Mater. Renew. Sustain. Energy*, 2015, **4**, 11.
37 C. Han, P. Su, B. Tan, X. Ma, H. Lv, C. Huang, P. Wang, Z. Tong, G. Li, Y. Huang and Z. Liu, *J. Colloid Interface Sci.*, 2021, **581**, 159–166.
38 Y. Yu, W. Yan, X. Wang, P. Li, W. Gao, H. Zou, S. Wu and K. Ding, *Adv. Mater.*, 2018, **30**, 1705060.
39 C. Lee, L. Hung, Y. Shih, J. Wu, S. Wang, C. Huang and V. Nguyen, *J. Environ. Chem. Eng.*, 2021, **9**, 104826.
40 M. Zhu, F. Zhang and Y. Wang, *New J. Chem.*, 2022, **46**, 16243–16255.
41 P. Sudhagar, A. Devadoss, K. Nakata, C. Terashima and A. Fujishim, *J. Electrochem. Soc.*, 2015, **162**(3), 108–114.
42 H. Le, M. Nguyen, Y. Pham, D. Nguyen, L. Le, H. Han and P. Tran, *Mater. Today Energy*, 2021, **21**, 100762.
43 S. Kumar, S. Ahirwarc and A. Satpati, *RSC Adv.*, 2019, **9**, 41368.
44 Y. Chen, Y. Chen, J. Chen, F. Cao, L. Li, Z. Luo, I. Leu and Y. Pu, *ACS Appl. Mater. Interfaces*, 2019, **11**, 8126–8137.
45 J. Yang, W. Liao and J. Wu, *ACS Appl. Mater. Interfaces*, 2013, **5**, 7425–7431.
46 R. Zhang, M. Shao, S. Xu, F. Ning, L. Zhou and M. Wei, *Nano Energy*, 2017, **33**, 21–28.
47 Y. Hwang, C. Hahn, B. Liu and P. Yang, *ACS Nano*, 2012, **6**, 5060–5069.
48 A. Dey, G. Chandrabosea, L. Dampteya, E. Erakulanb, R. Thapa, S. Zhukc, G. Dalapatia, S. Ramakrishnad, N. Braithwaitea, A. Shirzadia and S. Krishnamurthy, *Appl. Surf. Sci.*, 2020, **541**, 148571.
49 I. Daskalakis, I. Vamvasakis, I. Papadas, S. Tsatsos, S. Choulis, S. Kennouc and G. Armatas, *Inorg. Chem. Front.*, 2020, **7**, 4687.
50 K. Alam, P. Kumar, P. Kar, U. Thakur, S. Zeng, K. Cui and K. Shankar, *Nanoscale Adv.*, 2019, **1**, 1460–1471.
51 S. Kang, S. Li, T. Pu, X. Fang, C. Yin, M. Dong and L. Cui, *Int. J. Hydrogen Energy*, 2018, **43**, 22265–22272.
52 S. Zhang, Z. Liu, W. Yan, Z. Guo and M. Ruan, *Chin. J. Catal.*, 2020, **41**, 1884–1893.
53 B. Seger, T. Pedersen, A. Laursen, P. Vesborg, O. Hansen and I. Chorkendorff, *J. Am. Chem. Soc.*, 2013, **135**, 1057–1064.
54 E. Cowell, N. Alimardani, C. Knutson, J. Jr, D. Keszler, B. Gibbons and J. Wager, *Adv. Mater.*, 2011, **23**, 74–78.
55 Z. Bai, X. Yan, Y. Li, Z. Kang, S. Cao and Y. Zhang, *Adv. Energy Mater.*, 2016, **6**, 1501459.
56 M. Feng, Y. Liu, N. Wei, S. Ma, Z. Li, H. Li, S. Chen, J. Liu and D. Wang, *J. Mater. Chem. A*, 2018, **6**, 18293–18303.
57 D. Ma, Z. Wang, J. Shi, Y. Zou, Y. Lv, X. Ji, Z. Li, Y. Cheng and L. Wang, *J. Mater. Chem. A*, 2020, **8**, 11031–11042.
58 Y. Chen, Y. Chen, J. Chen, F. Cao, L. Li, Z. Luo, I. Leu and Y. Pu, *ACS Appl. Mater. Interfaces*, 2019, **11**, 8126–8137.
59 Z. Luo, T. Wang, J. Zhang, C. Li, H. Li and J. Gong, *Angew. Chem., Int. Ed.*, 2017, **56**(42), 12878–12882.
60 X. Zheng, Y. Wang, S. Ren, Q. Gai, W. Liu and Q. Dong, *ACS Appl. Energy Mater.*, 2022, **5**, 5756–5765.
61 Z. Zhang, Q. Qian, B. Li and K. Chen, *ACS Appl. Mater. Interfaces*, 2018, **10**, 17419–17426.
62 J. Yan, Z. Song, H. Li, H. Xu and L. Lee, *Chem. Eng. J.*, 2021, **425**, 131512.
63 H. Nan, W. Wu, K. Feng, B. Shan, Y. Qiu and Y. Zhang, *Int. J. Hydrogen Energy*, 2017, **42**, 848–857.
64 L. Steier, I. Herraiz-Cardona, S. Gimenez, F. Santiago, J. Bisquert, S. Tilley and M. Grätzel, *Adv. Funct. Mater.*, 2014, **24**, 7681–7688.
65 X. Xiao, X. Wang, Y. Li, Y. Li, G. Sun and Y. Han, *Appl. Surf. Sci.*, 2023, **631**, 157577.
66 C. Liu, C. Zhang, G. Yin, T. Zhang, W. Wang, G. Ou, H. Jin and Z. Chen, *ACS Appl. Mater. Interfaces*, 2021, **13**, 13301–13310.
67 J. Kim, *Appl. Sci.*, 2018, **8**, 1402.
68 A. Ghobadi, T. Ulusoy, R. Garifullin, M. Guler and A. Okyay, *Sci. Rep.*, 2016, **6**, 30587.
69 S. Mali, C. Shim, H. Park, J. Heo, P. Patil and C. Hong, *Chem. Mater.*, 2015, **27**, 1541–1551.
70 Y. Wang, W. Bai, S. Han, H. Wang, Q. Wu, J. Chen, G. Jiang, Z. Zhao, C. Xu and Q. Huan, *Curr. Catal.*, 2017, **6**, 50–56.
71 S. Li, P. Zhang, X. Song and L. Gao, *ACS Appl. Mater. Interfaces*, 2015, **7**, 18560–18565.
72 R. Rather, S. Singh and B. Pal, *Appl. Catal., B*, 2017, **213**, 9–17.
73 M. Park, J. Jung, Y. Nam, J. Song, C. Jeong and J. Lee, *Thin Solid Films*, 2016, **616**, 550–554.
74 M. Park, J. Jung, S. Shin, J. Song, Y. Nam, D. Kim and J. Lee, *Thin Solid Films*, 2016, **599**, 54–58.
75 S. Chen, Y. Qi, Q. Ding, Z. Li, J. Cui, F. Zhang and C. Li, *J. Catal.*, 2016, **339**, 77–83.
76 M. Rehman, I. Akhtar, W. Choi, K. Akbar, A. Farooq, S. Hussain, M. Shehzad, S. Chun, J. Jung and Y. Seo, *Carbon*, 2018, **132**, 157–164.
77 Q. Cheng, M. Benipal, Q. Liu, X. Wang, P. Crozier, C. Chan and R. Nemanich, *ACS Appl. Mater. Interfaces*, 2017, **9**, 16138–16147.
78 S. Nayak and K. Parida, *Sci. Rep.*, 2019, **9**, 2458.
79 C. Sakdaronnarong, A. Sangjan, S. Boonsith, D. Kim and H. Shin, *Catalysts*, 2020, **10**, 320.
80 Z. Shen, M. Cheng, Y. Yuan, L. Pei, J. Zhong, J. Guan, X. Li, Z. Li, L. Bao, X. Zhang, Z. Yu and Z. Zou, *Appl. Catal., B*, 2021, **295**, 120274.
81 P. Zhao, Y. Li, L. Li, S. Bu and W. Fan, *J. Phys. Chem. C*, 2018, **122**, 10737–10748.
82 S. Wang, Y. Zhang, Y. Zheng, Y. Xu, G. Yang, S. Zhong, Y. Zhao and S. Bai, *Small*, 2023, **19**, 2204774.
83 S. Zheng, L. Han, X. Luo, L. Sun, N. L, Z. Zhang and X. Li, *Int. J. Energy Res.*, 2022, **46**, 4506–4515.
84 X. Wu, X. Wang, Y. Xie, N. Ren, J. Ma and P. Ning, *Appl. Catal., B*, 2022, **310**, 121325.
85 W. Yang, L. Zhang, J. Xie, X. Zhang, Q. Liu, T. Yao, S. Wei, Q. Zhang and Y. Xie, *Angew. Chem., Int. Ed.*, 2016, **55**(23), 6716–6720.
86 Y. Zhao, G. Chen, T. Bian, C. Zhou, G. I. N. Waterhouse, L. Z. Wu, C. H. Tung, L. J. Smith, D. O'Hare and T. Zhang, *Adv. Mater.*, 2015, **27**, 7824.

87 X. Chen, L. Liu, Z. Liu, M. A. Marcus, W. C. Wang, N. A. Oyler, M. E. Grass, B. Mao, P. A. Glans, P. Y. Yu, J. Guo and S. S. Mao, *Sci. Rep.*, 2013, **3**, 1510.
88 Y. Chen, Y. Chen, J. Chen, F. Cao, L. Li, Z. Luo, I. Leu and Y. Pu, *ACS Appl. Mater. Interfaces*, 2019, **11**, 8126–8137.
89 K. M. Alam, C. E. Jensen, P. Kumar, R. W. Hooper, G. M. Bernard, A. Patidar, A. P. Manuel, N. Amer, A. Palmgren, D. N. Purschke, N. Chaulagain, J. Garcia, P. S. Kirwin, L. C. T. Shoute, K. Cui, S. Gusarov, A. E. Kobryn, V. K. Michaelis, F. A. Hegmann and K. Shankar, *ACS Appl. Mater. Interfaces*, 2021, **13**, 47418–47439.
90 P. Neuderth, P. Hille, J. Schörmann, A. Frank, C. Reitz, S. Martí-Sánchez, M. De, M. Coll, J. Arbiol, R. Marschall and M. Eickhoff, *J. Mater. Chem. A*, 2018, **6**, 565.
91 M. Kim, B. Joshi, E. Samuel, H. Seok, A. Aldalbahi, M. Almoiqli, M. Swihart and S. Yoon, *Appl. Catal., B*, 2020, **271**, 118928.
92 K. Rasamani, Z. Li and Y. Sun, *Nanoscale*, 2016, **8**, 18621.
93 C. Chen, P. Chen, M. Basu, K. Yang, Y. Lu, C. Dong, C. Ma, C. Shen, S. Hu and R. Liu, *J. Mater. Chem. A*, 2015, **3**, 23466.
94 S. Chen, X. Lia, W. Zhou, S. Zhang and Y. Fang, *Appl. Surf. Sci.*, 2019, **466**, 254–261.
95 B. Zhang, T. Yu, Y. Liu, M. Feng, X. Li, W. Sun and D. Wang, *Chem. Eng. J.*, 2022, **429**, 132248.
96 J. Qiu, G. Zeng, M. Ge, S. Arab, M. Mecklenburg, B. Hou, C. Shen, A. Benderskii and S. Cronin, *J. Catal.*, 2016, **337**, 133–137.
97 X. Zhang, G. Lu, Y. Wu, J. Dong and C. Wang, *Catal. Sci. Technol.*, 2021, **11**, 5505.
98 X. Yu, J. Xie, Q. Liu, H. Dong and Y. Li, *J. Colloid Interface Sci.*, 2021, **593**, 133–141.
99 Y. Ben-Shahar, F. Scotognella, N. Waiskopf, I. Kriegel, S. Conte, G. Cerullo and U. Banin, *Small*, 2015, **11**(4), 462–471.
100 N. Hewa-Kasakarage, M. Kirsanova, A. Nemchinov, N. Schmall, P. El-Khoury, A. Tarnovsky and M. Zamkov, *J. Am. Chem. Soc.*, 2009, **131**, 1328–1334.
101 A. Thibert, F. Frame, E. Busby, M. Holmes, F. Osterloh and D. Larsen, *J. Phys. Chem. Lett.*, 2011, **2**, 2688–2694.
102 P. Tongying, V. Plashnitsa, N. Petchsang, F. Vietmeyer, G. Ferraudi, G. Krylova and M. Kuno, *J. Phys. Chem. Lett.*, 2012, **3**, 3234–3240.
103 W. Kim, J. Kim, S. Lee, S. Lee, J. Woo, K. Lee, W. Chae, S. Jeong, W. Bae, J. McGuire, J. Moon, M. Jeong and D. Lee, *Chem. Mater.*, 2016, **28**, 962–968.
104 M. Liu, C. Yang, M. Wang and X. Ma, *J. Phys. Chem. C*, 2021, **125**, 21341–21351.
105 J. Xiong, J. Di, J. Xia, W. Zhu and H. Li, *Adv. Funct. Mater.*, 2018, **28**(39), 1801983.
106 Y. Huang, L. Meng, W. Xu and L. Li, *Adv. Funct. Mater.*, 2023, **33**(47), 2305940.
107 K. Dai, L. Lu, C. Liang, G. Zhu, Q. Liu, L. Geng and J. He, *Dalton Trans.*, 2015, **44**, 7903–7910.
108 Z. Zhang, M. Choi, M. Baek, I. Hwang, C. Cho, Z. Deng, J. Lee and K. Yong, *Nano Res.*, 2017, **10**, 2415–2430.
109 R. Huang, Z. Qin, L. Shen, G. Lv, F. Tao, J. Wang and Y. Gao, *J. Mater. Chem. A*, 2023, **11**, 6217–6225.
110 E. W. Cowell, N. Alimardani, C. C. Knutson, J. F. Conley, D. A. Keszler, B. J. Gibbons and J. F. Wager, *Adv. Mater.*, 2011, **23**(1), 74–78.
111 M. Liu, C. Y. Nam, C. T. Black, J. Kamcev and L. Zhang, *J. Phys. Chem. C*, 2013, **117**, 13396.
112 B. Seger, T. Pedersen, A. B. Laursen, P. C. K. Vesborg, O. Hansen and I. Chorkendorff, *J. Am. Chem. Soc.*, 2013, **135**, 1057–1064.
113 S. Agrawal, A. Srivastava and G. Kaushal, *Semicond. Sci. Technol.*, 2022, **37**, 025004.
114 F. Li, J. Jian, S. Wang, Z. Zhang, X. Guan, Y. Xu and H. Wang, *Chem. Eng. J.*, 2023, **461**, 141872.
115 P. Zhao, Y. Li, L. Li, S. Bu and W. Fan, *J. Phys. Chem. C*, 2018, **122**, 10737–10748.
116 B. He, R. Liu, J. Ren, C. Tang, Y. Zhong and Y. Hu, *Langmuir*, 2017, **33**, 6719–6726.
117 X. Bao and L. Liu, *J. Power Sources*, 2014, **268**, 677–682.
118 X. Wu, X. Wang, Y. Xie, N. Ren, J. Ma and P. Ning, *Appl. Catal., B*, 2022, **310**, 121325.
119 X. Ning, W. Zhen, X. Zhang and G. Lu, *ChemSusChem*, 2019, **12**, 1410–1420.
120 H. Guo, B. Luo, J. Wang, B. Wang, X. Huang, J. Yang, W. Gong, Y. Zhou and X. Niu, *J. Mater. Chem. A*, 2020, **8**, 24655–24663.

